Highligths

- Near stoichiometric Ni_2MnGa thin films with different compositions have been studied.
- NM or modulated 5M or 7M martensitic structures have been identified.
- The hardness and the magnetization depend on the composition and the temperature.
- Mechanical and magnetic properties are strongly linked.

Thermo-magneto-mechanical properties of near stoichiometric Ni_2MnGa (Mn > Ga) thin films deposited by radio-frequency magnetron sputtering on Si substrate.

C. Rousselot [(a)], D. Bourgault [(b)] and P. Delobelle [(c)]

[(a)] Départ. MN2S, Institut FEMTO-ST, UMR CNRS 6174, Université de Franche Comté, 4 place Tharradin, BP 71427, 25211 Montbéliard, France.

[(b)] Départ. MCBT, Institut Néel, 25 Avenue des Martyrs, BP 166, 38042 Grenoble Cedex 9, France.

[(c)] Départ. DMA, Institut FEMTO-ST, UMR CNRS 6174, Université de Franche Comté, 24 Chemin de l' Epitaphe, 25000 Besançon, France.

Corresponding author: P. Delobelle, E-mail address: patrick.delobelle@univ-fcomte.fr

Keywords: Magnetic shape memory alloy, Sputtered Ni_2MnGa films, Micro-structure, Nano-indentation, Thermo-mechanical properties, Thermo-magnetic properties.

Abstract

Near stoichiometric annealed thin films (1.5 to 3 µm) of Ni_2MnGa alloy and whose compositions are such that the Martensitic Transformation Temperatures $T_{M(e/a)}$ are in the range -60 °C to 200 °C have been deposited by R.F. magnetron sputtering on SiO_2/Si substrate. Crystallographic structure characterization such as planar spacing $d_{(i)}$, Thermal Expansion Coefficient CTE and structural domain size $L_{(i)}^*$, has been realized by X-ray diffraction over a wide temperature range from 25 to 205 °C. The mechanical properties such that the Young's modulus (E) and hardness (H_B), have been measured by ultra-nano-indentation tests carried out from ambient temperature to 175 °C. SQUID-VSM magnetometer measurements from -263 °C to 127 °C allow to some magnetic characteristics: evolution of the magnetization M versus the temperature and the Curie temperature T_C. Three diffraction peaks which can be attributed to the tetragonal (NM) or modulated (5M or 7M) martensitic structures of polycrystalline films have been identified. At ambient temperature Ta, the calculated planar spacing $d_{(i)}$ associated to at least two diffraction peaks present a linear decreasing with $T_{M(e/a)}$. As a function of the temperature and for the austenitic state only one value of the CTE has been determined. On the contrary, for the martensitic state, two values have been extracted and whose change is close to $T_{M(e/a)}$. No evident signature has been observed at the vicinity of the Curie temperature. The Young' modulus and particularly the hardness are very dependent on the film composition, the temperature and the state of the microstructure. At room temperature H_B linearly decreases with $T_{M(e/a)}$. As a function of the temperature, for the martensitic state, E slightly decreases whereas H_B is almost constant. At the opposite, in the austenitic domain, E slightly increases and H_B linearly increases with the temperature. A phenomenological model has been proposed. The whole of the annealed films show a ferromagnetic behavior and from the thermomagnetic curves it has been shown that four distinct states can be observed: para or ferromagnetic austenite and para or ferromagnetic martensite. A transition on the magnetization, certainly due to a change of the martensitic crystal structure, occurs at the neighbourhood of T_C. Mechanical (H_B) and magnetic (M) properties are strongly linked and at Ta it has been shown that the M is a linear decreasing function of H_B.

1. Introduction

Heusler-type alloy families like Ni_2Mn-(Ga, Al, Sn, In), Co_2Ni-(Ga, Al) are a class of materials which possess a reversible martensitic phase transformation and exhibit a ferromagnetic behavior controllable by temperature, magnetic field, stress and their combinations [1-7]. During the last twenty years many studies have been performed on various aspects of these ferromagnetic shape memory alloys (FSMA) and particularly on the bulk material or thin films of Ni-Mn-Ga system, such as structural description [8-19], martensitic phase transformation [9, 14, 14, 16-20], ferro-paramagnetic transformation, magnetic field induced strain and the effect of magnetic fields on the martensitic phase transformation [10, 12, 15, 16, 21-26]. Hence, it has been found that martensitic and magnetic phase transformation temperatures, transformation enthalpy, magneto-crystalline anisotropy and saturation magnetization are highly dependent on the composition of the alloys [9, 20-22, 25-28]. Moreover, it has been observed that the ferromagnetic-paramagnetic transition influences the structural phase transformation [28-30]. In addition, for micro and nano electro-mechanical systems applications [31-34], many efforts have been made to use thin films technologies (magnetron sputtering, ion beam sputtering, pulsed laser deposition technique) to produce films of near stoichiometric crystalline Ni_2MnGa martensite with good properties and a shape memory effect as in the bulk material. However, the technological parameters of the deposition process, presently the power, the argon pressure, the sputtering time and the deposition temperature are very crucial with regard to the whole of the film properties: composition, crystal structure, mechanical and magnetic properties [10, 13, 15, 25, 35]. The type of the substrate, Si with or without buffer [8, 13, 16-19, 24, 25, 36, 37-39], alumina [9, 11, 14, 20, 40, 41], SiO_2 [9], Mo [21], MgO [23, 42, 43], NaCl [26], glass [9], quartz [9], piezo-material, the film thicknesses (10 nm up to 5 µm) [9, 11, 12, 14, 16, 20-23, 36, 38-39, 41- 43] and the annealing temperature (300 to 1000 °C) are three determinant parameters which strongly affect all films properties.

Despite all the numerous studies which are focused on different aspects of the microstructure of the Ni-Mn-Ga films and their functional properties for a given substrate and for some compositions close to the stoichiometric one, no detailed study has been carried out for a SiO_2/Si substrate (suitable for micro-device applications), different film compositions allowing a wide domain of martensitic transformation temperatures from about - 60°C to 200 °C and over a relatively large range of temperature from 25 °C to about 200 °C. Hence, the different elaborated film/substrate composites have been examined by Energy-Dispersive X-ray Spectroscopy (EDS) to obtain the chemical composition of each film, transmission electron microscopy (TEM) to observe the microstructure of the cross-section of some films, X-ray diffraction (XRD) at different temperatures to analyze the structure of the films and its changes, ultra-nano-indentation to determine the evolutions of the indentation modulus and the hardness during the different structural transformations and at last SQUID-VSM magnetometer experiments to obtain the ferromagnetic properties as a function of the temperature. Particular emphasis is given to the analysis of the results of the measurements of high temperature XRD, ultra-nano-indentation and magnetic experiments and the eventual relations between them correlated with the microstructural properties.

2. Experimental procedures

2.1 Sample fabrication

Thin films of Ni-Mn-Ga have been deposited onto (100) silicon substrate (thickness of 280 µm) with a radio-frequency (RF) magnetron sputtering equipment (Alliance Concept AC 450). Two kinds of substrate holders have been used for the elaboration of the films. One allows the samples to be cooled to about 20 °C and the other allows them to heat up to 600 °C with a coaxial resistive device. Before heating a residual pressure of 5×10^{-7} Pa was obtained in the reactor. In addition, the chamber has been pre-heated in order to lower undesirable residual gas which can oxidize samples during the substrate heating process. Before introduction of the gas the pressure was below 5×10^{-5} Pa and the working argon pressure has been kept constant at 1 Pa using a mass flow controller and a constant pumping rate of $10\ \mathrm{l.s^{-1}}$. The RF power applied to the target was 120 W and the distance between the target and the substrate has been fixed at 63 mm. Under these conditions a high sputtering rate of $60\ \mathrm{nm.min^{-1}}$ has been obtained and, before annealing, the as deposited films present a small compressive mean residual stress (-150 to 0 MPa) [16]. The different utilized targets have an initial chemical composition close (~± 2 %) to the stoichiometric one $Ni_{50}Mn_{25}Ga_{25}$ and have been prepared by hot pressed powder (H.P.P.) of high purity of Ni, Mn and Ga (99.9%, Lesker with three different targets: Lesk. 0, 1, 2) or by using a Bridgman method (B.M.; Laue Langevin Institute of Grenoble, ILL). Before deposition the substrates have been cleaned to alcohol and sputtered etched in argon atmosphere with a negative bias voltage of 140 V during ten minutes for partially reduce the native silicon oxide of the silicon substrate. Hence, native silicon oxide that lowers the diffusion process of the Si atoms was not totally removed (50 to 100 nm thick). One specimen has been deposited on a chromium buffer (~ 100 nm) on the SiO_2/Si substrate. In situ annealing of the as-deposited films has been performed in a vacuum of 5×10^{-5} Pa for 10 or 20 hours at 600 °C. For this thermal treatment the samples have directly been annealed in the chamber straight after the sputtering and without putting them back to the ambient atmosphere to limit the oxidation of the films. After the annealing treatment the film-substrate was naturally cooled down under vacuum until ambient temperature. Some experiments have also been carried out on a bulk single crystal of $Ni_{51.2}Mn_{26.1}Ga_{22.7}$ material.

2.2 Experimental methods

The deposited films have been investigated by several complementary experimental techniques such as: Energy Dispersive X-ray Spectroscopy (EDS), X-ray diffraction (XRD), transmission electron microscopy (TEM), ultra nano-indentation (UNHT) and for the magnetic properties by a vibrating sample magnetometer (VSM) or alternating gradient force magnetometer (SQUID).

The thickness of the films has been measured with a stylus surface profiler DEKTAK 3030 and has been fixed by the sputtering time to obtain thicknesses of 1.5, 2 or 3 µm. The chemical composition of the different films has been achieved by energy dispersive X-ray spectroscopy (EDS) with a Princeton Gamma-Tech. The voltage speeding up and the beam current were 15 kV and 0.6 A, respectively. With these conditions the integration time was 60 s that is enough to reach a correlation factor of one.

Crystallographic structure characterization has been performed by X-ray diffraction (XRD) with a PANalytical X'Pert Pro with a X'Celerator detector from $2\theta = 40$ ° to $2\theta = 50$ ° and a high temperature chamber HTK 1200 (Anton Paar) for XRD temperature measurements. The step size and the integration time were 0.008 ° and 100 s/step, respectively. A $CuK_{\alpha1}$ radiation source which emits with a voltage of 45 kV and an intensity of 35 mA through a germanium monochromator has been used. For temperature measurements the diffractograms have been recorded in a temperature range of 25°C to 205 °C with steps of 20 °C, a ramp of 5 $°C.min^{-1}$ and a waiting time before acquisition of 15 min. The experiments have been carried out under a flux of dry helium and as previously from $2\theta = 40$ ° to 50 ° with a step of $2\theta = 0.008$ ° and 100 seconds by step.

Micro and nano structures of three different films have been investigated by transmission electron microscopy (TEM) with a Philips CM30 at 300 keV. The films were separated from the silicon and then coated by EPON 812 resin. After that, cross section of 30 nm thick has been cut by ultra-microtomic method. Then, they have been put on copper grid of 400 meshes in order to be examined.

Nano-indentation tests have been performed on the films using a CSM (now Anton Paar) instrument equipped with a UNHT (Ultra Nano-indentation Hardness Tester) head and a Berkovich tip whose radius is of the order of 100 ± 20 nm. The samples have been gripped on a Peltier cell whose temperature range is 20 °C to 200 °C. Hence, indentation tests have been carried out from 25 °C to 175 °C with steps of 15 or 20 °C (T= 25, 40, 60, 80, ..., 160, 175 °C). For each film and each temperature the measurement sequence consists of 6 indentations with a 50 µm space between them. The tests were conducted following the progressive multi-cycles procedure (CMC) in load control. Hence, for each indention ten loading (P_{max} maximal load) - unloading (90% of P_{max}) sequences were applied. P_{max} follows a quadratic progression such that P_{max}= 200, 320, 690, 1300, 2140, 3240, 4580, 6160, 7990 and 10 000 µN. For each cycle the loading-unloading time has been fixed at 10 x 2= 20 s, thus the entire indentation time is 200 s. For a fixed temperature the maximum amplitude of the variations is of the order of ± 0.1 °C. Moreover, as further shown, due to its referencing system, the UNHT head virtually eliminates the effects of the thermal drift and consequently the different loading-unloading loops are closed and reversible even at 175 °C.

Magnetization M versus temperature (-263 °C < T < 277 °C) and magnetization loop (0 - 5 T) measurements have been performed using a SQUID-VSM magnetometer from Quantum Design equipped with the VSM oven option. For the M(T) acquisitions, an external magnetic field of H = 100 and 1000 Oe (1 Oe = 79.58 Am^{-1}) has been applied to the films in the temperature range of -263 to 277°C. Films have been prepared in a zero-field cooled state (ZFK) by cooling from 25 °C to -263 °C without magnetic field. Subsequently, the external field was applied and the magnetization responses have been recorded on increasing temperature up to 127 °C. Without removing the external field, i.e. in field cooled state (FC), data have been recorded from 127 °C up to -263 °C. Using oven option (25 °C < T < 277 °C), field cooled (FC) and field heated (FH) procedures were adopted.

3. Structural characterization of the films

3.1 Chemical composition of the different films

Globally EDS results show that the films elaborated from the four targets (Lesk. 0, 1, 2 and ILL) present different (but close) chemical compositions for Ni, Mn and Ga contents depending on the target and the wear of the target after several hours of sputtering. Comparing target and films compositions, we can observe an increase of the Ni content and a decrease of the Mn and Ga content in the films which may result from the different sputtering yield of the Ni, Mn and Ga elements, as observed in the literature [44, 45]. For the long cumulative sputtering times (> 15 h) and with the wear of the target the same tendency has been observed, i.e. an increase of the Ni content and a decrease of the Ga composition, the Mn content being approximately constant. The composition of the different studied films, the origin of the target (Lesk. or ILL), the films thicknesses e_f and the thermal treatment after deposition (t_{an}= 10 h or 20 h at T_{an}= 600 °C) are reported in Table I. Moreover, in the different figures of this paper a color code has been attributed for each tested film (see Table I). As an example, for the specimen N336, the whole of the results in the different representations (EDS, XRD, nano-indentation, magnetization) are reported with a red color. The results obtained on other films with different compositions but only tested at ambient temperature are represented with a black color.

It is well known that the martensitic transformation temperature T_M and the Curie temperature T_C were controlled by the chemical composition [17, 28, 29, 46, 47]. The T_M temperature exhibits a linear increase ([18, 28, 47], Eq.1b) and the Curie temperature a small decrease as a function of the e/a ratio, namely the valence electron concentration per atom (Eq.1a):

$$e/a = (10\ \text{Ni\%} + 7\ \text{Mn\%} + 3\ \text{Ga\%})/100 \qquad \text{(Eq.1a)}$$

$$\text{and} \quad T_{M(e/a)}\ (°\text{C}) = 702.5\ (e/a) - 5340 \qquad \text{(Eq.1b).}$$

X% represents the atomic concentration of the element X. For each studied film the e/a ratio and the $T_{M(e/a)}$ values calculated with Eqs.1a-b are reported in Table II. Hence, in this study, $7.519 < e/a < 7.883$, $-58\ °\text{C} < T_{M(e/a)} < 198\ °\text{C}$ and as $1.5\ \mu\text{m} < e_f < 3\ \mu\text{m}$ the transformation temperature $T_{M(e/a)}$ is not affected by the thickness of the different films [9, 11, 20, 22, 41], contrary to the films whose thicknesses are smaller than 0.5 µm [41-43].

3.2 Nanostructure of some films

The TEM studies allow us to determine the microstructure of the film cross section. Hence, for $T_{M(e/a)}$ greater than the ambient temperature T_a, the films without thermal treatment exhibit a very fine columnar structure (Fig.1a). A zoom of these columns reveals a disordered stacking of few needles (Fig.1b) which confirms the presence of a martensitic phase. In contrast, for $T_{M(e/a)} > T_a$, the films annealed at 600 °C (10 or 20 h) are completely recrystallized with an average grain diameter of about 100 to 200 nm and present a superstructure of martensite with about 2 nm space between planes (Fig.2). This picture has been obtained on a film whose composition is close to the one of the N333 specimen ($T_{M(e/a)}$ ~ 70 °C).

3.3 Crystalline structure of the different films (25 °C< T< 205 °C)

3.3.1 Results at ambient temperature (Ta)

Fig. 3 shows six examples of XRD diffraction patterns of different Ni-Mn-Ga thin films (-58 °C < $T_{M(e/a)}$ < 198 °C). The film deposited at room temperature (N338, $T_{M(e/a)}$ ~ 55 °C) exhibits a crystalline structure with a principal diffraction peak at $2\theta_{(0)}$= 43°. This pattern does not correspond to the (220) austenitic parent phase peak at 2θ= 43°9. Thus the film is in a martensitic state at ambient temperature, in agreement with the $T_{M(e/a)}$ value and the TEM image given in Fig. 1b. The asymmetry of the peak indicates a beginning of a splitting which corresponds to the occurrence of a martensitic structure with a weak grain texture (Fig. 1b). According to the simulations of the X-ray profiles given by Wedel et al. [48] and Pons et al. [49] on the three most probable martensitic structures, namely the body centered tetragonal phase (BCT), the modulated 5M and 7M phases, the crystalline structure seems to be tetragonal martensite with a preferential orientation of (200) (2θ= 42°96) [10] or $(00\underline{10})$, $(00\underline{14})$ (2θ= 43°02) [48]. The patterns of the annealed samples at 600 °C during 10 h or 20 h and when $T_{M(e/a)}$ > Ta (martensitic state as shown in Fig. 2) generally present two peaks: a small one at $2\theta_{(0)}$~ 42°9, thus close to the one of the as-deposited film or at $2\theta_{(1)}$~ 43°5 (observed for N251, N283 and N333 films), and a new well defined peak with higher intensity in the neighborhood of $2\theta_{(2)}$~ 44°25 (± 0.15°) depending on the composition of the films. As previously mentioned the peak at $2\theta_{(0)}$~ 43° corresponds to the diffraction of the (200) planes of the tetragonal martensite or to the one of the $(00\underline{10})$ planes of the 5M layered martensite [12, 48]. The one at $2\theta_{(1)}$~ 43°5 is attributed to the diffraction of the (220) planes of the 5M tetragonal martensite with c/a_t< 1 [18, 19, 27]. The principal peak in the vicinity of 2θ~ 44°25 certainly corresponds to the diffraction of the (202) planes of the 5M (c/a_t<1) layered tetragonal martensite [9, 14, 23, 27, 41]. The $(\underline{1}27)$ reflection of the 7M martensite is also a possibility [9, 34, 48-50]. Note that the formation of 5M martensite has been confirmed by the Selected Area Electron Diffraction pattern of a small area of the image reported in Fig.2 which shows the presence of 5 aligned spots characteristic of the 5M structure [12, 29, 50] (not given in this paper). When $T_{M(e/a)}$ is lower or close to the room temperature (austenitic state) only one peak at $2\theta_{(2)}$~ 44°1 corresponding to the diffraction of the (220) planes of the austenite is observed (Fig.3, N312) [10, 18, 19, 27]. Moreover according to the TEM image reported in Fig. 2, the narrowness of these different peaks corresponds to a well-defined structure with large grains (100 to 200 nm) in the out-of-plane direction of a part of the film cross-section. However, it is important to note that with the XRD technique it is not easy to unambiguously determine the exact structural state of these textured fine grain thin films of Ni-Mn-Ga materials.

In Fig. 4 the planar spacing $d_{(1)}$ and $d_{(2)}$ of the different films respectively calculated from the positions of the $2\theta_{(1)}$ (~ 43°5) and $2\theta_{(2)}$ peaks (~ 44°1) (Bragg's formula) are plotted as a function of the calculated transformation temperature $T_{M(e/a)}$ (Eqs. 1a-b). The $d_{(2)}$ spacing presents a linear decreasing with $T_{M(e/a)}$: 2.042 A° < $d_{(2)}$ < 2.054 A° when -58 °C < $T_{M(e/a)}$ <198 °C. These values are in good agreement with those reported by Besseghini et al [14] for $Ni_{51.4}Mn_{28.3}Ga_{20.3}$ films whose thicknesses are in the range 0.6 - 5 μm. Due to the small amplitude of the $2\theta_{(0)}$ peaks near 42°9 and consequently to the scattering in its position, it is not possible to propose, as for $d_{(1)}$ and $d_{(2)}$ (Eqs.2), an accurate evolution of $d_{(0)}$ versus the transformation temperature: 2.101 A° < $d_{(0)}$ < 2.108 A° for 55 °C <$T_{M(e/a)}$ < 125 °C (not represented in Fig.4). However, this spacing seems to be independent of $T_{M(e/a)}$ and equal to $d_{(0)Ta}$= 2.106 $\pm$ 2.7×10^{-3} A°. On the contrary, for the specimen N283, which has been deposited onto 100 nm of chromium (Table I) and for the films N251, N333, 43°5 < $2\theta_{(1)}$ < 43°57, thus 2.077 < $d_{(1)}$(A°) < 2.081 (Fig.4). This planar spacing shows, as for $d_{(2)}$, a decreasing with the transformation temperature (Fig.4). Note that all these values ($d_{(0)}$, $d_{(1)}$ and $d_{(2)}$) are consistent and relatively close to those reported by Aseguinolaza et al. [18, 19]. As a conclusion, concerning the dependence of $d_{(2)Ta}$ and $d_{(1)Ta}$ on the (e/a) ratio and on the transformation temperature $T_{M(e/a)}$, according to the representation in Fig.4 and the equation 1b, the following relations are proposed:

$$2.042 < d_{(2)Ta}(\mathring{A}) < 2.054 \quad \text{with} \quad d_{(2)Ta}\,(\mathring{A}) = -\,3.59 \times 10^{-2}(e/a) + 2.325$$

and $$\alpha^{C}_{(2)Ta} = \left(\frac{1}{d_{(2)}}\frac{\partial d_{(2)}}{\partial T_{M(e/a)}}\right)_{Ta} = -2.5 \times 10^{-5}\ °C^{-1} \quad \text{for } 2\theta_{(2)} \text{ close to } 44°2$$

(Eq.2a).

As previously mentioned for $d_{(0)Ta}$ and $d_{(1)Ta}$ we can write:

$$d_{(0)Ta} = 2.106 \pm \underline{2.7 \times 10^{-3}}\ (A°) \text{ for } 2\theta_{(0)} \sim 43° \text{ and}$$

$$2.077 < d_{(1)Ta}\ (A°) < 2.081 \quad \text{with} \quad d_{(1)Ta}\left(\mathrm{\mathring{A}}\right) = -\,3.13 \times 10^{-2}\ (e/a) + 2.323$$

$$\text{and} \quad \underline{\alpha^{C}_{(1)Ta} = \left(\frac{1}{d_{(1)}}\frac{\partial d_{(1)}}{\partial T_{M(e/a)}}\right)_{Ta} = -2.2 \times 10^{-5}\ °C^{-1}} \text{ for } 2\theta_{(1)} \text{ close to } 43°5 \qquad \text{(Eq.2b).}$$

In these equations the C exponent means composition. In agreement with the results of Ma et al. [51] obtained on $Ni_{50+x}Mn_{25}Ga_{25-x}$ bulk materials and for $x < 7$, a quasi linear increase of the transformation temperatures with the Ni content has presently been observed. So:

$$T_{M(e/a)}\ (°C) = 3244\ Ni\%/100 - 1648 \qquad \text{(Eq.2c).}$$

Indeed, for the whole of the different studied films Mn% > Ga% and in a first approximation it has been found that Mn% and Ga% are linearly dependent on the Ni concentration: Ga% ~ -0.534 Ni% + 50.56 and Mn% ~ -0.54 Ni% + 53.4. So, combining these relations with Eqs.1a, 1b the relation 2c can be deduced. Two factors are principally responsible of this dependence, first the increase with the Ni content of the electron concentration (e/a) and secondly the size factor (c/a) of the tetragonal martensite [51]. Combining Eqs. 1b, 2a and 2c it is easy to show that:

$$d_{(2)Ta}\left(\mathrm{\mathring{A}}\right) = -\,0.166\ Ni\%/100 + 2.134 \qquad \text{(Eq.2d).}$$

The same kind of relation could be obtained for the $d_{(1)}$ spacing. Hence, $d_{(2)Ta}$ (and $d_{(1)}$) presents a linear decreasing with the Ni content. In fact with $(c/a_t) < 1$, the lattice parameter a_t contracts while the c axis elongates [14, 51]. So, the relation 2d indicates that the preferential martensite variants present a long lattice parameter a_t parallel to the film plane.

3.3.2 High temperature XRD results.

As previously mentioned XRD measurements have been recorded in a temperature range of 25 °C to 205 °C by steps of 20 °C. Figures 5a,b report the evolutions of the planar spacing $d_{(2)}$ and $d_{(0)}$ or $d_{(1)}$ ($2\theta_{(0)} \sim 43°$ or $2\theta_{(1)} \sim 43°5$) as a function of reduced temperature ($T-T_{M(e/a)}$), respectively. So, when $T-T_{M(e/a)} > 0$ the films are in an austenitic state and at the opposite for $T-T_{M(e/a)} < 0$ in a martensitic one. The vertical arrows in Figs.5a,b correspond to the ($T_C-T_{M(e/a)}$) parameter where T_C is the Curie temperature determined, as further shown (section 5), using a SQUID-VSM magnetometer. So, on the right of these arrows a paramagnetic phase is obtained and on the left a ferromagnetic one. As expected, a change in the slopes of the different representations can be observed at the vicinity of $T\text{-}T_{M(e/a)}= 0$ [14, 16, 24]. Contrary to the results reported by Besseghini et al. [14] and Bernard et al. [15, 16, 24] no marked signature at the neighborhood of the Curie temperature T_C can be observed. Moreover at $T = T_{M(e/a)}$ the $d_{(2)TM}$ spacing exhibits a very weak change with the transformation temperature such that:

$$\alpha^{C}_{(2)T_M} = \left(\frac{1}{d_{(2)T_M}}\frac{\partial d_{(2)T_M}}{\partial T_{M(e/a)}}\right) \sim 6 \text{ to } 8 \times 10^{-6}\ {}^{\circ}\mathrm{C}^{-1} \text{ with a mean value equal to:}$$

$$d_{(2)TM(e/a)}= 2.052 \pm 1.6 \times 10^{-3}\ \text{A°} \qquad \text{(Eq. 3).}$$

Due to the spread of the $d_{(0)TM}$ and $d_{(1)TM}$ experimental values it is not possible to extract a potential evolution with $T_{M(e/a)}$ but the mean values are equal to: $d_{(0)TM(e/a)}= 2.105 \pm 3 \times 10^{-3}$ A° when $2\theta_{(0)} \sim 43°$ and $d_{(1)TM(e/a)}= 2.084 \pm 1.5 \times 10^{-3}$ A° when $2\theta_{(1)} \sim 43°5$.

The out-of-plane Coefficient of Thermal Expansion (CTE) α^{Th} of the different phases (austenite, martensite in paramagnetic or ferromagnetic state) is calculated from the slopes of the quasi-linear segments of the $d_{(i)} = f(T\text{-}T_{M(e/a)})$ representations (Figs. 5a,b):

$$\alpha^{Th}_{(i)SN} = \left(\frac{1}{d_{(i)}}\frac{\partial d_{(i)}}{\partial T}\right)_{T_{M(e/a)}} \quad i = 0, 1, 2\ , \text{ with: S= A}$$

$$\text{(austenite), M(martensite) and N= P (paramagnetic), F (ferromagnetic)} \qquad \text{(Eq. 4a)}$$

or with an incremental algorithm between two measurements with ΔT= 20 °C (Fig.6) and such that:

$$\alpha^{Th}_{(i)T_{mean}} = \frac{2}{\Delta T}\frac{d_{(i)\,J+\Delta T} - d_{(i)\,J}}{d_{(i)\,J+\Delta T} + d_{(i)\,J}} \text{ with } T_{mean} = \frac{T_{J+\Delta T} + T_J}{2}\text{, J= 25, 45, ..., 205 °C} \qquad \text{(Eq.4b).}$$

From these different figures several values of the CTE have been extracted, thus:

$$\alpha^{Th}_{(0)AP/F} \sim \alpha^{Th}_{(1)AP/F} \sim \alpha^{Th}_{(2)AP/F} = 2.4 \pm 0.3 \times 10^{-5}\ {}^{\circ}\mathrm{C}^{-1}\ ,\ \alpha^{Th}_{(0)MP/F} \sim \alpha^{Th}_{(1)MP/F} = 1.4 \pm 0.4 \times 10^{-5}\ {}^{\circ}\mathrm{C}^{-1} \text{ and } \alpha^{Th}_{(2)MP/F} = 5 \pm 0.5 \times 10^{-5}\ {}^{\circ}\mathrm{C}^{-1}$$

As previously mentioned no evident transition has been observed at the neighborhood of the Curie temperature. Note that the value of $\alpha^{Th}_{(1)AP/F}$ is close to the one obtained on as deposited film (N338, Fig. 5b) whose structure has been identified as paramagnetic martensite at room temperature. As expected, for the cubic symmetry of the austenitic phase, $\alpha^{Th}_{(1)A} \sim \alpha^{Th}_{(2)A}$ and consequently no anisotropic behavior is observed. Moreover, in the austenitic state, the value of the CTE is in a good agreement with those reported by Aseguinolaza et al. [18, 19], $\alpha^{Th}_{A} = 2.3 \text{ x } 10^{-5}\,{}^{\circ}C^{-1}$, Bernard et al.[16], $\alpha^{Th}_{A} = 2.7 \text{ x } 10^{-5}\,{}^{\circ}C^{-1}$ and in a less extent by Besseghini et al. [14] for ferromagnetic austenite, $\alpha^{Th}_{AF} = 3 \pm 1 \text{ x } 10^{-5}\,{}^{\circ}C^{-1}$. However in the paramagnetic state these last authors have reported a value of $\alpha^{Th}_{AP} = 1.5 \pm 0.1 \text{ x } 10^{-5}\,{}^{\circ}C^{-1}$ thus close to the one of $\alpha^{Th}_{(1)MP/F}$ for the martensitic phase in the present study. This observation is not yet understood. For the martensitic state the $\alpha^{Th}_{(1)MP/F}$ value is close to the one reported by Bernard et al. [16], $\alpha^{Th}_{MP} = 1.6 \text{ x } 10^{-5}\,{}^{\circ}C^{-1}$ and as previously mentioned equal to α^{Th}_{AP} for the paramagnetic austenitic phase [11]. The $\alpha^{Th}_{(2)MP/F}$ value is consistent with those measured by Besseghini et al. [14] and Bernard et al. [15, 16, 24], $\alpha^{Th}_{MF} = 5 \pm 2 \text{ x } 10^{-5}\,{}^{\circ}C^{-1}$ and $4 \text{ x } 10^{-5}$ °C^{-1}, respectively. Note that the CTE value along the c axis of the tetragonal lattice reported by Aseguinolaza et al. [18, 19] is equal to $9.5 \text{ x } 10^{-5}$ °C^{-1}.

It is interesting to note that $\alpha^{Th}_{(1)A} \sim \alpha^{Th}_{(2)A} \sim -\alpha^{C}_{(1)T_a} \sim -\alpha^{C}_{(2)T_a}$. Thus for the evolution $d(d_{(1)})$ and $d(d_{(2)})$ of the planar spacing, a variation ΔT of the temperature in the austenitic state is equivalent to the same negative variation $-\Delta T_M$ of the transformation temperature at ambient temperature. In other terms:

$$d\left(d_{(i)}\right) = \alpha^{Th}_{(i)A} d(T - T_M) = -\alpha^{C}_{(i)Ta}\, d(T_a - T_M),\ i = 1, 2 \qquad \text{Eq.5.}$$

The structural domain size L^* has classically been extracted from the value of the full width at half maximum (FWHM) of the diffraction peak using the Scherrer formula. Hence, in Fig.7 the $L^*_{(2)}$ domain size corresponding to the $2\theta_{(2)}$ peak ($d_{(2)}$ spacing) has been plotted as a function of the reduced temperature $T\text{-}T_{M(e/a)}$. As reported by Besseghini at al. [14] the $L^*_{(2)}$ behavior is rather complex but perfectly reversible with the temperature and several transitions can be observed. So, $200 < L^*_{(2)} < 700$ nm thus greater than $L^*_{(0)}$ ($2\theta_{(0)}$ peak) calculated for the as deposited film (Fig.7) showing the increasing after the annealing of the nanocrystal dimension with the one of the grain diameter. Due to the small amplitude of the $2\theta_{(0)}$ peaks reliable values of $L^*_{(0)}$ cannot be determined. The variation of $L^*_{(1)}$ calculated for the N283 film has also been represented in Fig.7. Out-of-plane coefficients of thermal variation of the structural domain $\Delta^{C}_{(2)}$ and $\Delta^{Th}_{(2)}$ (CTEL), as in Eq.3a for $d_{(i)}$, have been calculated:

$$\Delta^{C}_{(2)} = \left(\frac{1}{L^{*}_{(2)}} \frac{\partial L^{*}_{(2)}}{\partial T_{M(e/a)}}\right)_{T_a}, \quad \Delta^{Th}_{(2)} = \left(\frac{1}{L^{*}_{(2)}} \frac{\partial L^{*}_{(2)}}{\partial T}\right)_{T_{M(e/a)}} \qquad \text{Eq.6.}$$

As a function of the composition $\Delta^{C}_{(2)} \sim -1.\ \mathrm{x}\ 10^{-3}\ ^{\circ}C^{-1}$ with $220 < L^{*}_{(2)} < 380$ nm. For $\Delta^{Th}_{(2)}$ several situations have to be considered. If $T_{M(e/a)} < T_{MC} = 69$°C, so $T_a\text{-}T_{MC} = -45$ °C, whatever the state of the films (austenitic or martensitic), $T\text{-}T_{M(e/a)} > T_a\text{-}T_{MC}$ in Fig.7, $\Delta^{Th}_{(2)} \sim 1.\ \mathrm{x}\ 10^{-3}\ ^{\circ}C^{-1}$ thus equal to $-\Delta^{C}_{(2)}$, as for the $\alpha^{Th}_{(2)}$ CTE. At the opposite, when $T_{M(e/a)} > T_{MC}$ and in the martensite state, two possibilities can be observed in Fig.7. If $T\text{-}T_{M(e/a)} < T_a\text{-}T_{MC}$, $\Delta^{Th}_{(2)M} \sim 1.\ \mathrm{x}\ 10^{-3}\ ^{\circ}C^{-1}$, as previously calculated, and when $T\text{-}T_{M(e/a)} > T_a\text{-}T_{MC}$, $\Delta^{Th}_{(2)M} \sim 7\ \mathrm{x}\ 10^{-3}\ ^{\circ}C^{-1}$. For the austenitic phase, of course when $T\text{-}T_{M(e/a)} > 0$, $\Delta^{Th}_{(2)A} \sim 3.6\ \mathrm{x}\ 10^{-3}\ ^{\circ}C^{-1}$. Moreover, for the N283 film, as shown in Fig.7, approximately the same values can be calculated for $\Delta^{Th}_{(1)M}$ but with $L^{*}_{(1)M} > L^{*}_{(2)M}$. It is interesting to remark that when $T_{M(e/a)} > T_{MC}$, $\Delta^{Th}_{(2)M}/\Delta^{Th}_{(2)A} \sim \alpha^{Th}_{(2)M}/\alpha^{Th}_{(2)A} \sim 2$ with $\Delta^{Th}_{(2)M}/\alpha^{Th}_{(2)M} = \Delta^{Th}_{(2)A}/\alpha^{Th}_{(2)A} \sim 150$. Hence, the variations of the structural domain size are directly linked to those of the lattice spacing of the different phases, thus reversible with the temperature. Note that the values of the CTEL previously reported are consistent with those which can be calculated from the paper of Besseghini and al. [14]: $\Delta^{Th}_{AP} \sim 1.3\ \mathrm{x}\ 10^{-3}\ ^{\circ}C^{-1}$, $\Delta^{Th}_{AF} \sim 6$ to $9\ \mathrm{x}\ 10^{-3}\ ^{\circ}C^{-1}$ and $\Delta^{Th}_{MF} \sim 1.\ \mathrm{x}\ 10^{-3}\ ^{\circ}C^{-1}$, but not for the same state. The interpretation of the T_{MC} temperature could be attributable to the hysteresis between the start and the finish of the M-> A transformation which is, according to the work of Ma et al. [51], an increasing function of the Ni content. However, the T_{MC} value (~70 °C) is too high to validate this hypothesis. More likely, following Lanska et al. [29] and Dai et al. [30] when T_M is greater than T_C only NM tetragonal crystal structure can be obtained and at the opposite when T_M is lower than T_C the three 7M, 5M and NM classical structures can simultaneously be observed. Hence, the transition at the vicinity of $T_{MC} \sim T_M \sim T_C$ observed on the structural domain size $L^{*}_{(i)}$ could be associated with a change in the martensite crystal structure. This point will be mentioned and discussed in the next sections (4 and 5). Indeed, according to Besseghini et al. [14] the detailed feature of the reversible temperature dependence of the $L^{*}_{(2)}$ parameter is not totally understood.

4. Thermo mechanical properties (25 °C <T< 175 °C)

As previously mentioned ultra-nanoindentation tests (UNHT) have been carried out on the different films at ambient and high temperatures (25°C <T< 175°C) following a multi-cycles procedure (CMC) in load control (section 2.2). Hence, from the unloading path of each cycle and according to the Oliver and Pharr [51, 52] relations, the indentation modulus M or the Young modulus E if the Poisson ratio ν is known ($E= M(1-\nu^2)$) and the Berkovich hardness H_B can be determined. Among the numerous results the Fig.8 shows four complete indentation curves (N336), load P versus the penetration depth h (10 cycles) for four different temperatures. The maximum depth is in the range 250 nm to 350 nm and for the whole of the films $h/e_f < 20\%$. The inset gives a magnified view of the four first cycles which correspond to relatively low penetration depths, smaller than 80 nm. Note that due to its referencing system the UNHT head eliminates the effects of the thermal drift, even at 175 °C and for very small penetrations, h < 80 nm, the loading-unloading loops are closed and reversible (Fig.8). On each sample and for a given temperature six indentations have been performed. The mean measured values of the indentation modulus and of the hardness versus the indentation depth slightly decrease (~ 10%) until 80 to 100 nm (4 first cycles) and then are constant for the remaining indentation depths. Thus, the substrate effect is negligible for these small indentation depths. These constant values have been considered as the measure of M and H_B and sensibly correspond to $5\ \% < h/e_f < 10\ \%$. At ambient temperature the roughness of the films is in the range 1.5 to 2 nm and consequently the standard deviation on the indentation modulus $\Delta M/M$ is about 2.9 % for h = 100 nm and 1.4 % for h = 300 nm [54]. For the evaluation of the Young's modulus value a Poisson ratio of ν = 0.25 has been considered.

4.1 Results at ambient temperature

The whole of the values of the Young's modulus E and of the hardness H_B determined on numerous films (different compositions and thicknesses with and without annealing, this study and in ref. [16]) have been plotted in Fig. 9. Obviously these values greatly depend on the composition (austenitic or martensitic states), the thickness, the sputtering conditions and the thermal treatment of the different films. Hence, globally, 90 GPa < E < 150 GPa and 4 GPa < H_B < 9 GPa. Note that all these values are located in a $E = f(H_B)$ delimited space (dashed line in Fig. 9) which converge toward a zone corresponding to those obtained on the bulk crystal: E = 85 GPa and H_B = 3.7 GPa. Note that these two values are very close to those reported by Ohtsuka et al. [40] for bulk material: E = 81 GPa and H_B = 3.6 GPa. However, for the thin films, very few results are reported in the literature: Jetta et al. [17] (E = 133 GPa, H_B = 7 GPa), Liu et al. [36] (E = 155, 125 GPa, H_B = 5.5, 4.2 GPa, respectively) for as deposited films, Ohtsuka et al. [40] for two compositions (50 % and 52 % of Ni) and different annealing temperatures (600 °C to 900 °C) during 3.6 ks (H_B = HUT/73) and Kumar et al. [39] for films deposited at different temperatures (300 to 550 °C). These different values have been reported in Fig.9 and are consistent with those measured in the present study. The higher values essentially correspond to as deposited films with very fine columnar micro-structure (few nanometers) and at the opposite the lower to well annealed films with larger grains (few hundred nanometers). The deposition parameters, thicknesses (1.5 - 3 µm) and annealing conditions (10 or 20 h at 600 °C) are close to each other and consequently the principal variable parameter is the composition of the films. Thus in Fig.10 the hardness at ambient temperature T_a and for $T = T_{M(e/a)}$ (see next section Fig.12b) has been plotted as a function of the reduced temperature T_a-$T_{M(e/a)}$. Clearly, in the martensitic state, the hardness is an increasing function of T_a-$T_{M(e/a)}$, 4.5 GPa < H_B < 8.5 GPa for -180 °C < T_a-$T_{M(e/a)}$ < -30 °C, thus according to the relations 1b and 2c a decreasing function of the e/a ratio and of the Ni content. To simplify, a bilinear evolution can be drawn in Fig. 10 and such that:

$$\left(\frac{\partial H_{B(M)}}{\partial T_{M(e/a)}}\right)_{T_a} = -\frac{\partial H_{B(M)}}{\partial (T_a - T_{M(e/a)})} = -23 \text{ MPa°C}^{-1} \text{ if } T_{M(e/a)} > T_{MC}\, , \ (T_a - T_{MC}) < -45\,°\text{C}$$

and $$\left(\frac{\partial H_B}{\partial T_{M(e/a)}}\right)_{T_a} = -46 \text{ MPa°C}^{-1} \text{ if } T_{M(e/a)} < T_{MC}\, . \qquad \text{Eq.7.}$$

As previously mentioned in section 3.3.2, T_{MC} ~ 69 °C could be associated to a change in the martensitic structure. As shown in Fig.4, the planar spacing $d_{(2)}$ is a decreasing function of $T_{M(e/a)}$ and consequently, according to the relations (7), should be an increasing function of the hardness: the $d_{(2)}$ and $d_{(1)}$ spacing have been plotted as a function of the hardness H_B in Fig.11. Hence, for the martensitic state at ambient temperature, a quasi-linear evolution is reported and such that:

$$\left(\frac{\partial d_{(i)}}{\partial H_{B(M)}}\right)_{T_a} = 2.15 \times 10^{-3} \text{ Å GPa}^{-1}\, , \ i = 1, 2 \qquad \text{Eq.8.}$$

Note that:

$$\left(\frac{\partial H_B}{\partial T_{M(e/a)}}\right)_{T_a} = \left(\frac{\partial d_{(2)}}{\partial T_{M(e/a)}}\right)_{T_a} / \left(\frac{\partial d_{(2)}}{\partial H_{B(M)}}\right)_{T_a} = \alpha^{C}_{(2)T_a} d_{(2)} \left(\frac{\partial H_{B(M)}}{\partial d_{(2)}}\right)_{T_a} = -2.38 \times 10^{-2}\ \mathrm{GPa°C^{-1}}$$

thus close to - 24 MPa°C^{-1}. Eq.9.

This value is consistent with those given in relations (7), particularly to -23 MPa°C^{-1} for $T_{M(e/a)} > T_{MC}$. The transition at the neighbourhood of T_{MC} in the $H_B = f(T_a - T_{M(e/a)})$ representation is not obvious on the $d_{(2)}$ spacing. Note that about the same value has been calculated with the $d_{(1)}$ spacing: -21 MPa°C^{-1}.

Now, considering the generalized Tabor's relation [55], the mean stress σ corresponding to the hardness H_B is given by: $H_B = 3\sigma$. Hence from Eq.(7), $(\partial\sigma / \partial T_{M(e/a)})_{T_a}$ ~ - 7.7 MPa°C^{-1} and - 15.3 MPa°C^{-1} with a mean value equal to – 11.5 MPa°C^{-1}, whose absolute values are relatively close to the classical value of the $(\partial\sigma / \partial T_M)$ ~ 10 MPa°C^{-1} term in the Clapeyron relation (Eq.10a) for bulk shape memory alloys:

$$T^*_M = T_M + \left(\frac{\partial T_M}{\partial \sigma}\right)\sigma \quad \text{with } (\partial T_M/\partial\sigma) = 0.1\ \mathrm{°CMPa^{-1}} \qquad \text{Eq.10a.}$$

The negative sign, as observed by L'vov et al. [41, 59] for compression tests, is due to the compressive nature of the stress during the indentation test. As the relation (10a) is independent of the mode of creation of non-zero stress, taking the hardness into account, this relation can be recasted as:

$$T^*_{M(e/a)} = T_{M(e/a)} - \left(\frac{\partial T_{M(e/a)}}{\partial H_{B(M)}}\right)_{T_a} H_{B(M)} \qquad \text{Eq.10b}$$

with $-(\partial H_{B(M)} / \partial T_{M(e/a)})_{T_a} = 23 \text{ or } 24\ \mathrm{MPa°C^{-1}}$ (Eqs.7 or 9). Taking into account that the minimum value of the hardness is equal to H_{B0} = 3.5 GPa, the $T^*_{M(e/a)}$ temperature has been calculated for the different experimental points. Quasi-constant values have been obtained: $T^*_{M(e/a)}$ = 233 ± 16 °C and 225 ± 12°C, respectively. Hence, $H_{B(M)} = H_{B0} - \left(\frac{\partial H_{B(M)}}{\partial T_{M(e/a)}}\right)(T^*_{M(e/a)} - T_{M(e/a)})$. So, for a confined zone under the indenter, the induced stress is proportional to $-(\partial H_{B(M)} / \partial T_{M(e/a)}) T_{M(e/a)}$, thus only dependent on the composition of the films according to the relations (1a,b). The proportionality factor is consistent to the one of the Clapeyron equation reported for this kind of bulk shape memory alloys. In Fig.10 this corresponds to a translation of $(T^{*}_{M(e/a)} - T_a)$ of the different experimental points. It can be remarked that for bulk materials, Ma et al. [51] have reported a constant value of the transformation temperature equal to 440 °C when the Ni content exceeds 0.57. Presently, with $T^{*}_{M(e/a)} = 225\,°C$ the relation (2c) gives 0.577, thus in good agreement with the previous value. Therefore, $T^{*}_{M(e/a)}$ corresponds to the maximum of the transformation temperature value which can be induced by the composition or the stress.

4.2 High temperature indentation results.

As described in section 2.2, ultra-nanoindentation tests have been carried out on the different films until a temperature of 175 °C. An example of indentation curves P = f(h) for four temperatures on the N336 specimen is reported in Fig.8. From these representations it seems obvious that the mechanical properties evolve with the temperature and particularly the hardness as the indentation depth decreases with the temperature for a same load: the hardness increases with the temperature. The variations with the reduced temperature ($T-T_{M(e/a)}$) of the Young's modulus E ($\nu = 0.25$) and the hardness H_B have been reported in the Fig.12a,b respectively. Note that the relative standard deviations $\Delta E/E$ and $\Delta H_B/H_B$ determined on six indents are quasi-linear increasing functions of the temperature and such that: $\Delta E/E$ = 1.4 %, 3.9 %, 5.3 % and $\Delta H_B/H_B$ = 2 %, 4.6 %, 7.7 % for T= 25 °C, 100 °C and 160 °C, respectively. The Young's modulus (Fig.12a) slightly decreases (~ - 0.12 ± 0.05 GPa°C^{-1}) in the martensitic domain until a temperature slightly lower than $T_{M(e/a)}$ and close to T_{MC} and then increases (0.21 ± 0.04 GPa°C^{-1}) before to saturate in the austenitic state. Note that the minimum is located between T_{MC} and $T_{M(e/a)}$ and could be associated to the change in the martensitic structure of the films. For the high values of $T-T_{M(e/a)}$ the Young's modulus values saturate toward 135 GPa to 155 GPa. The hardnesses (Fig.12b) are quasi-constant, thus independent of the temperature in the martensitic state ($T-T_{M(e/a)} < 0$), excepted a very slight increase at the vicinity of T_{MC} and then strongly increase as soon as $T > T_{M(e/a)}$ until about 10.5 GPa in the austenitic domain. The mean value of the slope is such that:

$$\left(\frac{\partial H_{B(A)}}{\partial T}\right)_{T_M} = 25.5 \pm 5\ \mathrm{MPa°C^{-1}}\ \text{thus}\ \left(\frac{\partial \sigma}{\partial T}\right)_{T_M} = 8.5 \pm 1.7\ \mathrm{MPa°C^{-1}} \qquad \text{Eq.11.}$$

As for the CTE ($\alpha^{Th}_{(i)A} = -\alpha^{C}_{(i)T_a}$), in the austenitic state, the same kind of relation is observed on the hardness (Eqs.7 and 11):

$$\left(\frac{\partial H_{B(A)}}{\partial T}\right)_{T_M} = -\left(\frac{\partial H_{B(M)}}{\partial T_{M(e/a)}}\right)_{T_a} \sim 24 \pm 1.5\ \mathrm{MPa^\circ C^{-1}} \qquad \text{Eq.12.}$$

The mean induced stress during the penetration of the indenter into the martensitic phase is quasi-independent of the temperature as in a classical Ni base alloy for a moderate range of temperature close to the room temperature. On the contrary, in the austenitic domain ($T-T_{M(e/a)} > 0$), the induced stress greatly increases to locally transform the austenite into martensite respecting the relations (10). Hence, for a given isotherm and for $T > T_{M(e/a)}$, the increasing of the hardness ΔH_B verify the equation (10b) with $T_M^* = T$:

$$T_M^* = T = T_{M(e/a)} - \left(\frac{\partial T_{M(e/a)}}{\partial H_B}\right)_{T_{M(e/a)}} \Delta H_B \qquad \text{Eq.13.}$$

So, to resume the previous observed behavior of the hardness, the following relations (Eqs. 14a to d) are proposed:

If $T = T^*_{M(e/a)}$ then $H_{B(M)} = H_{B0} = 3.5\ \mathrm{GPa}$.

If $T_{M(e/a)} > T_a$ and $T < T_{M(e/a)}$ then $H_{B(M)} = H_{B0} - \left(\frac{\partial H_{B(M)}}{\partial T_{M(e/a)}}\right)(T^*_{M(e/a)} - T_{M(e/a)})$ Eq.14a

or when $T > T_{M(e/a)}$ it is easy to show that:

$$H_{B(A)} = H_{B(M)} - \frac{\partial H_{B(M)}}{\partial T_{M(e/a)}}\left(T - T_{M(e/a)}\right) = H_{B0} - \left(\frac{\partial H_{B(M)}}{\partial T_{M(e/a)}}\right)\left(T + T^*_{M(e/a)} - 2T_{M(e/a)}\right) \qquad \text{Eq.14b}$$

When $T_{M(e/a)} < T_a$, due to the lack of experimental results, it is more difficult to propose unquestionable relation. However, the results given by Kumar et al. [39] ($T_{M(e/a)}$ has been calculated thanks to the relations 1a,b) have been reported in Fig.13 and converge with those of the present study, particularly for the austenitic state. Thus, at $T=T_a$ and for the same value of the hardness in matensitic and austenitic states, considering the symmetry with respect to $T_a = T_{M(e/a)}$ (see specimen N312 and the results of Kumar et al. [39] in Fig.10), for $T < T_{M(e/a)}$ the following equation can be written:

$$H_{B(A)} = H_{B0} - \left(\frac{\partial H_{B(A)}}{\partial T_{M(e/a)}}\right)\left(T^*_{M(e/a)} - \left|T_{M(e/a)}\right| - 2T_a\right) \qquad \text{Eq.14c.}$$

Moreover, for $T > T_{M(e/a)}$ and taking the increasing of the hardness with the temperature (Fig.12b) into account, the relation (14d) can be deduced:

$$H_{B(A)} = H_{B0} - \left(\frac{\partial H_{B(A)}}{\partial T_{M(e/a)}}\right)(\,T + T^{*}_{M(e/a)} - |T_{M(e/a)}| - 3T_a\,)$$ Eq.14d.

Quantitatively, with $-(\frac{\partial H_{B(M)}}{\partial T_{M(e/a)}})_{T_a} = 2.4 \times 10^{-2}\,GPa°C^{-1}$ and $T^{*}_{M(e/a)} = 225\ °C$, the values of the hardness calculated with the previous relations (Eqs.14a-d) are in a fairly good agreement with the experimental results. As examples, the results calculated with the previous relations for the N312, N336 and NE1 films have been drawn on Fig.12b. Now, in Fig.13, to take the simultaneous variations of E and H_B with the temperatures T and $T_{M(e/a)}$ into account, the $H_B/3E$ parameter, assimilable to a plastic resistance parameter or a `indentation deformation' ε_B^{Pl} (~ σ/E), has been plotted as a function of the reduced temperature ($T-T_{M(e/a)}$). Two straight lines can be drawn and such that: $(\partial(H_B/3E)/\,\partial(T - T_{M(e/a)}))_{T_M} = (\partial(H_B/3E)\,/\,\partial T)_{T_M} \sim 1.7 \pm 0.2 \times 10^{-5}\ °C^{-1}$ in the martensitic domain and ~ $3.8 \pm 0.5 \times 10^{-5}\ °C^{-1}$ for the austenitic one. The mean indentation deformation range ε_B^{Pl} is 1.2 % to 2.5 %. The small variation of the hardness observed at the vicinity of T_{MC} is not obvious and seems to be suppressed. Note that $\frac{\partial(H_B/3E)}{\partial(T-T_{M(e/a)})} = -\frac{\partial(H_B/3E)}{\partial T_{M(e/a)}} \sim 8 \times 10^{-5}\ °C^{-1}$ and $13 \times 10^{-5}\ °C^{-1}$ at $T = T_a$ and $T = T_{M_{(e/a)}}$, respectively. In fact these three values could be deduced from the different quantities previously estimated. Hence, as a first approximation:

$$\frac{\partial(H_B/3E)}{\partial(T-T_M)} = \frac{\partial\varepsilon_B^{Pl}}{\partial(T-T_M)} \sim \frac{1}{3E_{mean}}\left(\frac{\partial H_B}{\partial(T-T_M)} - \frac{H_{Bmean}}{E_{mean}}\frac{\partial E}{\partial(T-T_M)}\right)$$ Eq.15.

H_{Bmean} and E_{mean} are the mean values of the hardness (~ 6.5 GPa) and of the Young's modulus (= 130 GPa) and with $(\partial H_B/\,\partial(T - T_{M(e/a)}))_{T_M} = 0$ or $2.4 \times 10^{-2}\ GPa°C^{-1}$ and $(\partial E/\,\partial(T - T_{M(e/a)}))_{T_M} = -0.12$ or $0.21\ GPa°C^{-1}$ (values previously reported), the relation (15) gives: 1.5 x 10^{-5}, 3.6 x 10^{-5} and 8.8 x 10^{-5} $°C^{-1}$, thus close to those determined from the Fig.13. So, the slope in the martensitic domain (1.7 x 10^{-5} $°C^{-1}$) is essentially due to the decreasing of the Young's modulus with the temperature.

For a given isotherm T, the difference between this temperature and the one of the transformation T_M, function of the composition and of the stress, is the fundamental parameter which controls the state of the material. However, in this study, the T_M temperature has not experimentally been determined, Differential Scanning Calorimetry, resistivity experiments or other, but deduced thanks to the relations (1a,b) from the composition of the films (EDS measurements). The uncertainties on the determination of the percentage of each element, particularly on the gallium component, and the degree of exactness of the relation (1b), condition the precision of the $T_{M(e/a)}$ values. Nevertheless, the inter-planar spacing $d_{(i)}$ have experimentally been determined by XRD and as $d_{(i)}$ depend on the composition of the films (Eqs.2), on the intrinsic and extrinsic stresses and on the temperature (Eq.5), it should be interesting to analyze the relation between the mean plastic indentation deformation ε_B^{Pl} ($H_B/3E$) and the $d_{(i)}$ spacing. This has been done in the Fig.14 with the $d_{(2)}$ spacing and the same kind of representation that the one of the Fig.13 has been obtained. In fact, if the calculated $T_{M(e/a)}$ values are sufficiently accurate and according to the equality (5) the following relation should be verified:

$$d\left(d_{(i)}\right) = \beta\, d(T - T_M) \text{ with } \beta = \alpha^{Th}_{(i)A} = -\alpha^{C}_{(i)T_a} \text{ or } \alpha^{Th}_{(i)M} \qquad \text{Eq.16.}$$

Thus, the two quantities $d_{(i)}$ and (T-T_M) give two equivalent possibilities to describe the thermo-mechanical properties of these thin films.

As a conclusion, the thermo-mechanical properties of this FSMA are drastically dependent on the composition of the films (via the T_M temperature), the microstructural state of the material (austenitic or martensitic and the nature of the martensite) and the reduced temperature T-T_M. At the opposite, for a given composition, the mechanical properties are weakly sensitive to the magnetic state of the film (para or ferromagnetic).

5. Thermo magnetic properties (-263 °C< T< 277 °C)

Examples of magnetization curves $M = f(H_m)$ measured on specimens N335 and N336 at different increasing temperatures and for applied magnetic field H_m in the range $\pm$ 5 x 10^4 Oe have been reported in Fig.15a. A zoom for relatively small applied fields ($\pm$ 4 x 10^3 Oe) of the previous curves (N335 specimen) and the magnetization loops for H_m in the range $\pm 10^3$ Oe are given in Fig.15b. According to the results of the literature [10, 15, 16], the whole of the annealed films show ferromagnetic behavior, contrary to the as deposited one where no ferromagnetic hysteresis occurs. At room temperature and for relatively small fields ($|H_m| <$ 4 x 10^3 Oe), the magnetization varies as the root square of the applied magnetic field as shown in the Fig. 15b:

$$M\ (\mathrm{emu/cm^3}) = \alpha \sqrt{|H_m|}\ \frac{H_m}{|H_m|} \text{ with } \alpha = 3.92\ \mathrm{emu/cm^3Oe^{1/2}} \qquad \text{Eq.17.}$$

This relation will be further used at the end of this section.

Thermo magnetic curves of the different films recorded for two magnetic fields, H_m= 100 and 1000 Oe, have respectively been reported in Figs. 16a,b. Hence, the magnetization M has been plotted as a function of the reduced temperature ($T-T_{M(e/a)}$). Note that the systematic splitting observed between the zero-field cooled state (ZFC) and the field-cooled state (FC) curves (not reported), essentially exhibited in the martensite state, can be interpreted by exchange bias effects and magnetic glass properties. Indeed, in Ni-Mn Heusler alloys, such phenomena can be explained with the hypothesis that Mn atoms, bearing the major magnetic moment in the cell, couple together anti-ferromagnetically at short range in addition to their ferromagnetic coupling *[57, 58].* In Figs.16, the curves essentially reveal a ferro-paramagnetic transition by a sudden drop in the magnetization. This transition occurs for the martensitic or the austenitic states. The Curie temperature T_C determined by the tangent method (see Figs.16) slowly decreases with the martensitic transformation temperature $T_{M(e/a)}$, or the e/a ratio, from 111 °C to 80 °C (Table II). The Curie temperature T_C can be greater or lower than the transformation temperature $T_{M(e/a)}$ (Figs.16) and consequently four distinct states can be expected: para or ferromagnetic austenite and para or ferromagnetic martensite. Note that $T_C \sim T_{M(e/a)} \sim 81$ °C for e/a ~ 7.71, in a good agreement with the literature [28]. Moreover, in Figs. 16 no appreciable signature of structural transition near $T = T_{M(e/a)}$ can be observed, in agreement with some works [9, 19, 22, 25]. Nevertheless, as shown in Fig.17a where the magnetization for two isotherms (T = -250 °C and 25°C) and H_m= 100 and 1000 Oe has been reported as a function of $T_C-T_{M(e/a)}$ temperature, an obvious transition occurs at the neighborhood of $T_C = T_{M(e/a)}$ or more exactly when $T_C = T_{M(e/a)} = 81$ °C and $T_C-T_{MC} = 12$ °C ($T_{MC} = 69$ °C). Hence, for T = -250 °C a ratio of about two on the magnetization characterizes this transition. As previously mentioned and following Lanska et al. [29] when T_M is greater than T_C, or e/a > 7.71, only NM tetragonal crystal structure ($c/a_t > 1$) can be obtained and at the opposite when T_M is lower than T_C the three classical different structures, 7M, 5M and NM ($c/a_t < 1$), can be observed. Thus, for a given isotherm, the transition of the magnetization in the ferromagnetic state measured at the vicinity of $T_M \sim T_{MC} \sim T_C$ is probably due to the change of the crystal structure. The magnetization for the NM structure is thus higher than the one of the mixture of 5M or 7M and NM structures. Note that if T_C is determined at the inflexion of the decreasing of the M(T) curves, the T_C values are about 10 to 13 °C lower than those previously reported and consequently with this method the transition occurs at $T_{MC} = T_C$. It is interesting to remark that the behavior of the magnetization as a function of T_C-$T_{M(e/a)}$ is comparable to the one of the structural domain size L^*, previously presented in section 3.3.2, which sensibly shows the same dependence and a transition at the vicinity of $T_C = T_{M(e/a)}$. Globally for a given isotherm the magnetization is a decreasing function of the structural domain size L^*.

As previously mentioned the planar spacing $d_{(i)}$ and the reduced temperature (T-$T_{M(e/a)}$) are two equivalent ways to describe the thermo-mechanical properties of these films and consequently it should be judicious to analyze the dependence of the magnetization M as a function of the $d_{(2)}$ spacing. This has been done in Fig. 17b for two isotherms (25 °C and 45 °C) and the evolution is conform to the one drawn in Fig.17a. An obvious transition occurs at $d_{(2)}$= 2.0488 A° and 2.0498 A° for T = 25 °C and 45 °C, respectively. Mechanical and magnetic properties are greatly dependent on the microstructure of the films which is presently function of the characteristic temperatures, $T_{M(e/a)}$, T_C or T_{MC}. Hence, these two properties must eventually be linked by a quantitative relationship. In Fig.18 the magnetization M at T = 25 °C and 45 °C and for the two applied magnetic fields H_m has been plotted as a function of the hardness H_B. Except for the two specimens NE1 and N330 which are exactly localized at the transition temperature T_{MC}, linear decreasing evolutions have been obtained. So at the vicinity of the ambient temperature, $(\partial M/\partial H_B)_T$=-22.4 emu/cm^{3}GPa and -62.4 emu/cm^3 GPa for H_m = 100 Oe and 1000 Oe, respectively. Moreover, as previously mentioned, for the relatively small magnetic fields (IH_mI < 3000 Oe), the magnetization M evolves as the root square of IH_mI (Fig.15b) and consequently, the following relation can be proposed (Fig. 18b):

$$M/\sqrt{H_m}\,(\text{emu/cm}^3\ \text{Oe}^{1/2}) = 20.16 - 2.22 H_B\ (\text{GPa}) \qquad \text{Eq.(18a).}$$

The results reported by Kumar et al. [39] for a magnetic field of H_m = 500 Oe have also been represented in Fig. 18b and are in a fairly good agreement with the equation 18a. Taking the Tabor's relation into account the equation (18a) can be recasted as:

$$M = M_0\sqrt{\frac{|H_m|}{H_{mo}}}\left(1-\frac{|\sigma|}{\sigma_0}\right)\frac{H_m}{|H_m|} \qquad \text{Eq.18b.}$$

with M_0 = 32 emu/cm^3, H_{m0} = 2.5 Oe and σ_0= 3.03 GPa.

To conclude this section and as expected, the whole of the annealed films exhibits a ferromagnetic behavior. Moreover, the magnetic and the mechanical properties which are very dependent on the structural material parameters such as planar spacing and domain size are close connected and exhibit a quasi linear decreasing relationship (Eqs. 18 and Figs. 18).

6. Conclusions

Near stoichiometric Ni_2MnGa annealed thin films have been deposited by R.F. magnetron sputtering on SiO_2/Si substrate. The martensitic transformation temperatures $T_{M(e/a)}$ have been calculated from the e/a electron concentration per atom determined thanks to EDS measurements and are in the range -58 °C to 198°C. Crystallographic structural characterization: planar spacing $d_{(i)}$, thermal expansion coefficient (CTE) $\alpha_{(i)}^{Th}$ and structural domain size $L_{(i)}^*$, has been obtained by X ray diffraction analysis carried out from 25 to 205 °C. Three different peaks whose indexation corresponds to the tetragonal NM or modulated, 5M or 7M, martensitic structures of polycrystalline films have been identified. At ambient temperature the planar spacing $d_{(i)}$ associated to at least two peaks show a linear decreasing dependence $T_{M(e/a)}$. The CTE for the austenitic state is equal to $\alpha_{(i)A}^{Th} = 2.4 \times 10^{-5}$ °C^{-1}. Two values have been measured for the martensitic state, 1.4×10^{-5} °C^{-1} and 5×10^{-5} °C^{-1}. Any evident signature has been observed at the vicinity of the Curie temperature T_C. The mechanical properties such that the Young's modulus (E) and hardness (H_B), have been determined by ultra-nano-indentation tests performed from ambient temperature to 175 °C. The Young's modulus and particularly the hardness are very dependent of the film composition C, the temperature T and the state of the microstructure: $110 < E(C,T) < 152$ GPa and $4.4 < H_B(C,T) < 10.5$ GPa. Hence, at room temperature, H_B linearly decreases with $T_{M(e/a)}$ (~ -24 MPa°C^{-1}). As a function of the temperature, for the martensitic state, E slightly decreases whereas H_B is weakly sensitive. At the opposite, in the austenitic domain, E slightly increases whereas H_B linearly increases with the temperature (~ 25 MPa°C^{-1}). A fairly simple phenomenological model has been proposed. SQUID-VSM measurements from -263 °C to 127 °C allow the evolution of the magnetization M and the determination of the Curie temperature T_C to be obtained. The whole of the annealed films present a ferromagnetic behavior. Hence, as function of the temperature four distinct states can be obtained: para or ferromagnetic austenite and para or ferromagnetic martensite. A transition on the magnetization, certainly due to a change of the martensitic crystal structure, occurs at the neighborhood of $T_C \sim T_M$. Mechanical (H_B) and magnetic (M) properties are strongly linked and at ambient temperature M presents a linear decreasing dependence on H_B. The whole of the presented results have also been analyzed as a function of the planar spacing $d_{(i)}$ parameter.

Acknowledgment

The authors express their gratitude to F. Bernard for X-ray measurements performed at room temperature on some specimens. This work has partially been supported by the French Research Ministry under the MAPHENIX ANR project (2011RMNP 0051), The Pays Montbéliard Agglomeration (PMA) and corresponds to a synthesis of the main results obtained over about the past ten years.

References

[1] R.C. O’ Handley, S.M. Allen in M. Schwartz Ed. Encyclopedia of SMART materials. Wiley, New York, 2002.

[2] O. Heczko, N. Scheerbaum, O. Gutfleisch, Magnetic Shape Memory Phenomena, Chap. 14, in Nanoscale magnetic materials and application, Ed. J. Ping Liu, E. Fullerton, O. Gutfleisch, D.J. Sellmyer, (2009) Springer US, 399-439.

[3] S.Fahler, Why Magnetic Shape Memory Alloy ?, Advanced Engineering Material, 2012, 14, 8, Wiley-VCH Verleg GmbH&Co.

[4] E. Cesari, J. Pons, R. Santamarta, C. Segui, V.A. Chernenko, Ferromanetic shape memory alloys : an overview, Arch. Metall. Mat. 49 (4) (2004) 779-789.

[5] E. Cesari, J. Pons, C. Segui, V.A. Chernenko, New ferromagnetic shape memory systems: in H. Moraviec, D. Stroz Eds.. Applied Crystallophaphy. World Scientific, (2004) 128-133.

[6] L. Righy, F. Albertini, S. Fabbrici, A. Paoluzi, Crystal Structure of Modulated Martensitic Phases of FSM Heusler Alloy, in Material Science Forum, Ed. V.A. Chernenko, 684.

[7] V.A. Chernenko, S. Besseghini, Ferromagnetic shape memory alloys: scientific and applied aspects, Sensors and Actuators A 142 (2008) 542-548.

[8] S.K. Wu, K.H. Tseng, J.Y. Wang, Crystallization behavior of rf-sputtered near stoichiometric Ni_2MnGa thin films, Thin Solid Films 408 (2002) 316-320.

[9] V. A. Chernenko, M. Ohtsuka, M. Kohl, V.V. Khovailo, T. Takagi, Transformation behavior of Ni-Mn-Ga thin films, Smart Mater. Struct. 14 (2005) 5245-5252.

[10] H. Rumpf, C.M. Craciunescu, H. Modrow, K. Olimov, E. Quandt, M. Wuttig, Successive occurrence of ferromagnetic and shape memory properties during crystallization of NiMnGa freestanding films, J. Magnetism and Magnet. Mat. 302 (2006) 421-428.

[11] V. Chernenko, M. Kohl, S. Doyle, P. Mûllner, M. Ohtsuka, Texture and transformation characteristics of Ni-Mn-Ga films deposited on alumina, Scripta Met. 504 (2006) 1287-1291.

[12] V.A. Chernenko, R. Lopez Anton, M. Kohl, J.M. Barandiaran, M. Ohtsuka, I. Orue, S. Besseghini, Structural and magnetic characterization of martensitic Ni-Mn-Ga thin films deposited on Mo foil, Acta Mater. 54 (2006) 2561-2567.

[13] F. Bernard, C. Rousselot, L. Hirsinger, P. Delobelle, Characterisation of ferromagnetic shape memory alloy Ni_2MnGa deposited by RF magnetron sputtering, Plasma Process Polym. 4 (2007) 5846-5850.

[14] S. Besseghini, T. Cavallin, V. Chernenko, E. Villa, V. Lvoc, M. Ohtsuka, Variation of atomic spacing and thermomechanical properties in Ni-Mn-Ga/alumina films composites, Acta Mater. 56 (2008) 1797-1801.

[15] F. Bernard, P. Delobelle, L. Hirsinger, C. Rousselot, Structural and mechanical characterisations of Ni-Mn-Ga thin films deposited by R.F. sputtering and heat-treated, Mat. Sci. Forum Vol. 583 (2008) 213-228.

[16] F. Bernard, P. Delobelle, C. Rousselot, L. Hirsinger, Microstructural, mechanical and magnetic properties of shape memory alloy $Ni_{55}Mn_{23}Ga_{55}$ thin films deposited by radio-frequency magnetron sputtering, Thin Solid Films 518 (2009) 399-412.

[17] N. Jetta, N. Ozdemir, S. Rios, D. Bufford, I. Karaman, X. Zhang, Phase transformations in sputtered Ni-Mn-Ga magnetic shape memory alloy thin films, Thin Solid Films 520 (2012) 3433-3439.

[18] I.R. Aseguinolaza, I. Reyes-Ssalazar, A.V. Svalov, K. Wilson, W.B. Knowlton, P. Müllner, J.M. Barandiaran, E. Villa, V.A. Chernenko, Transformation volume strain in Ni-Mn-Ga thin films, Appl. Phys. Lett. 101, 241912 (2012) 1-4.

[19] I.R. Aseguinolaza, I. Orue, A.V. Svalov, K. Wilson, P. Müllner, J.M. barandiaran, V.A. Chernenko, Martensitic transformation in Ni-Mn-Ga/Si(100) thin film, Thin Solid Films 558 (2014) 449-454.

[20] V.A. Chernenko, M. Kohl, V.A. L'vov, V.M.Kniazkyi, M. Ohtsuka, O. Kraft, Martensitic transformation and microstructure of sputtered deposited Ni-Mn-Ga films, Mat. Trans. 47 (3) (2006) 619-624.

[21] M. Kohl, A. Agarwal, V.A. Chernenko, M. Ohtsuka, K. Seemann, Shape memory effect and magnetostriction in polycrystalline Ni-Mn-Ga thin film microactuators, Mat. Sci. Eng. A 438-440 (2006) 940-943.

[22] S. Besseghini, A. Gambardella, V.A. Chernenko, M. Hagler, C. Pohl, P. Müllner, M. Ohtsuka, S. Doyle, Transformation behavior of Ni-Mn-Ga/Si(100) thin film composites with different thicknesses, Eur. Phys. J. Special Topics 158 (2008) 179-185.

[23] V.A. Chernenko, S. Besseghini, M. Hagler, P. Müllner, M. Ohtsuka, F. Stortiero, Properties of sputter-deposited Ni-Mn-Ga thin films, Mat. Sci. Eng. A 481-482 (2008) 271-274.

[24] F. Bernard, C. Rousselot, P. Delobelle, L. Hirsinger, P. Burdet, Magnetic-field induced strains in ferromagnetic shape memory alloy $Ni_{55}Mn_{23}Ga_{22}$ deposited by R.F. magnetron sputtering, Plasma Process. Polym. 6 (2009) 5822-5825.

[25] A. Annadurai, A.K. Nandakumar, S. Jayakumar, M. J. Kannan, M. Manivel Raja, S. Bysak, R. Gopolan, V. Chandrasebaran, Composition, structure and magnetic properties of sputter deposited Ni-Mn-Ga ferromagnetic shape memory thin films, J. Magnetism and Magnet. Mat. 321 (2009) 630-634

[26] I.R. Aseguinolaza, V. Golub, J.M. Barandiaran, M. Ohtsuka, P. Müllner, O.Y. Salyuk, V.A. Chernenko. Martensitic transformation and magnetic anisotropy of Ni-Mn-Ga/NaCl(001) thin films probed by ferromagnetic resonance, Appl. Phys. Lett. 102 (2013) 182401.

[27] B. Ingale, R. Gopalan, M. Manivel Raja, V. Chandrasekaran, S. Ram, Magnetostructural transformation, microstructure, and magnetocaloric effect in Ni-Mn-Ga Heusler alloys, J. Appl. Phys. 102, 013906 (2007) 1-5.

[28] P. Entel, V.D. Buchelnikov, M.E. Gruner, A.Hucht, V.V. Khovailo, S.K Nayak, A.T. Zayak, Shape memory alloys: a summary of recent achievements, Mat. Sci. Forum vol.583 (2008) 21-41.

[29] N. Lanska, O. Söderberg, A. Sozinov, Y. Ge, K. Ullakko, V.K. Lindroos, Composition and temperature dependence of the crystal structure of Ni-Mn-Ga alloys, J. Appl. Phys. 95, 12 (2004) 8074-8078.

[30] L. Dai, J. Cullen, M. Wuttig, Intermartensitic transformation in NiMnGa alloy, J. Appl. Phys. 98, 11 (2004) 6957-6959.

[31] J. Marcos, L. Manosa, A. Planes, F. Casanova, X. Batlle, A. Lakarta, Multiscale origin of the magnetocaloric effect in Ni-Mn-Ga shape memory alloys, Phys. Rev. B 68 (2003) 094401.

[32] Y. Fu, H. Du, W. Huang, S. Zhang, M. Hu, TiNi based thin films in MEMS application : a review, Sensors and Actuators A 112 (2004) 395-408.

[33] M. Kohl, D. Brugger, M. Ohtsuka, T. Takagi, A novel actuation mechanism on the basis of ferromagnetic SMA thin films, Sensors and Actuators A 114 (2004) 445-450.

[34] M. Kohl, D. Brugger, M. Ohtsuka, B. Krevet, A ferromagnetic shape memory actuator designed for 2D optical scanning, Sensors and Actuators A: Phys. 135 1 (2007) 92-98.

[35] C. Liu, W. Cai, X.An, L.X. Gao, Z.Y. Gao, L.C. Zhao, Preparation and characterization of Ni-Mn-Ga high temperature shape memory alloy thin films using rf magnetron sputtering method, Mat. Sci. Eng. A 438-440 (2006) 986-989.

[36] C. Liu, Z.Y. Gao, X. An, H.B. Wang, L.X. Gao, W. Cai, Surface characteristics and nanoindentation study of Ni-Mn-Ga ferromagnetic shape memory sputtered thin films, Appl. Surf. Sci. 254 (2008) 2861-2865.

[37] M. Wuttig, C. Craciunescu, J. Li, Phase transformations in ferromagnetic NiMnGa shape memory films, Mat. Trans. 41, 8 (2000) 933-937.

[38] A. Sharma, S. Mohan, S. Suwas, Development of bi-axial preferred orientation in epiaxial NiMnGa thin films and its consequence on magnetic properties, Acta Mater. 113 (2016) 259-271.

[39] V. Vinodh Kumar, M. Mahendran, M. Manivel Raja, V.L. Niranjani, P.K. Mukhopadhyay, Phase structure evolution on Ni-Mn-Ga/Si (100) thin films: Effect of substrate temperature, Intermetallics 101 (2018) 18-26.

[40] I. Ohtsuka, M. Matsumoto, K. Itagaki, Mechanical and shape memory properties of ferromagnetic Ni_2MnGa sputter-deposited films, J. Phy. IV 112 (2003) 899-902.

[41] V.A. Chernenko, M. Kohl, M. Ohtsuka, T. Takagi, V.A. L'vov, V.M. Kniazkyi, Thickness dependence of transformation characteristics of Ni-Mn-Ga thin films deposited on alumina: Experiment and modeling, Mat. Sci. Eng. A 438-440 (2006) 944-947.

[42] P. Ranzieri, S. Fabbrici, L. Nasi, L. Righi, F. Casoli, V.A. Chernenko, E. Villa, F. Albertni, Epitaxial Ni-Mn-Ga/MgO (100) thin films ranging in thickness from 10 to 100 nm, Acta Mater. 61 (2013) 263-272.

[43] A. Auge, N. Teichert, M. Meinert, G. Reiss, A. Hutten, E. Yuzuak, I. Dincer, Y. Elerman, I. Ennen, P. Schattschneider, Thickness dependence of martensitic magnetism and magnetoresistance in epitaxial NiMnSn ultra-thin films, Phys. Review B, 85, (2012) 214118.

[44] M. Suzuki, M. Ohtsuka, M. Matsumoto, Y. Murakami, D. Shindo, K. Itagaki, Effect of aging time on shape memory properties of sputtered Ni rich Ni_2MnGa alloy films, Mat. Trans. 43, 5 (2002) 861-866.

[45] S.K. Wu, K.H. Tseng, Composition control of R.F. sputtered Ni_2MnGa thin films using optical emission spectroscopy, Mat. Trans. 43, 5 (2002) 871-875.

[46] S.K. Wu, S.T. Yang, Effect of composition on transformation temperature of Ni-Mn-Ga shape memory alloys, Mat. Letters 57 (2003) 4291-4296.

[47] X. Jin, M. Marioni, D. Bono, S.M. Allen, R.C. O'Handley, T.C. Hsu, Empirical mapping of Ni-Mn-Ga properties with composition and valence electron concentration, J. Appl. Phys. 91 (2002) 8222.

[48] B. Wedel, M. Suzuki, Y. Murakami, C. Wedel, ST. Suzuki, D. Shindo, K. Itagaki, Low temperature crystal structure of Ni-Mn-Ga alloys, J. Alloys Compounds, 290 (1999) 137-143.

[49] J. Pons, V.A. Chernenko, R. Santamarta, E. Cesari, Crystal structure of martensitic phases in Ni-Mn-Ga shape memory alloys, Acta Mater. 48 (2000) 3027-3038.

[50] V.A. Chernenko, R. Lopez Anton, M. Kohl, M. Ohtsuka, I. Orue, J.M. Barandiaran, Magnetic domains in Ni-Mn-Ga martensitic thin films, J. Phys. Condens. Mater. 17 (2005) 5215-5224.

[51] Y. Ma, C. Jiang, Y. Li, H. Xu, C. Wang, X. Liu, Study of $Ni_{50+x}Mn_{25}Ga_{25-x}$ (x=2-11) as high temperature shape-memory alloys, Acta Mater. 55 (2007) 1533-1541.

[52] W.C. Oliver, G.M. Pharr, An improved technique for determining hardness and elastic modulus using load and displacement sensing indentation experiments, Mat. Res. 7 (1992) 1564-1583.

[53] J.J. Vlassak, W.D. Nix, Measuring the elastic properties of anisotropic materials by means of indentation experiments, J. Mech. Phys. Solids 42 (1994) 1223-1245.

[54] M. Qasmi, P. Delobelle, Influence of the average roughness Rms on the precision of the Young's modulus and hardness determination using nanoindentation technique with a Berkovich indenter, Surf. Coat. Techn. 201 (2006) 1191-1199.

[55] D. Tabor, The hardness of metals, Clarendon Press, Oxford 1951.

[56] V.A. L'vov, V.A. Chernenko, Thermodynamics of stress induced martensitic transformation: application ti Ni-Mn-Ga alloys, Eur. Phys. J.: Appl. Phys. 8 (1999) 25-28.

[57] E. Kren, E. Nagy, I. Nagy, L. Pal, P. Szabo, Structure and phase transformations in MnNi system near equiatomic concentration, J. Phys. and Chem. of Sol. 29 (1) (1968) 101-108.

[58] J.S. Kasper, J.S. Kouvel, The antiferromanetic structure of NiMn, J. Phys. and Chem. of Sol. 11 (3-4) (1959) 231-238.

Figures captions

Fig. 1: (a) TEM image in bright field mode of the cross section of a film deposited at room temperature (T_M>T_a) without thermal treatment. (b) High resolution image of a small area of the previous cross-section.

Fig. 2: High resolution view of a martensitic nanostructured grain of the cross-section of an annealed film (10 h at 600 °C). Presence of a martensitic superstructure as $T_{M(e/a)} > T_a$ (composition close to the one of the N333 specimen).

Fig. 3: XRD patterns at room temperature from 41° to 46° of six different films. Positions of the $2\theta_{(0)}$, $2\theta_{(1)}$ and $2\theta_{(2)}$ peaks. The vertical lines correspond to the simulated diffraction patterns (literature) of the most probable martensitic structures.

Fig. 4: Planar spacing $d_{(1)}$ and $d_{(2)}$ of the different films as a function of the transformation temperature $T_{M(e/a)}$.

Fig. 5: (a) Planar spacing $d_{(2)}$ of the different films as a function of the reduced temperature $T-T_{M(e/a)}$. The arrows correspond to $T_C-T_{M(e/a)}$. (b) Idem for the $d_{(0)}$ and $d_{(1)}$ spacing.

Fig. 6: Thermal expansion coefficients $\alpha_{(i)}^{Th}$ determined by an incremental algorithm (Eq. 4b) as a function of the reduced temperature $T_{mean}-T_{M(e/a)}$.

Fig. 7: Dependence on the structural domain size $L_{(2)}^*$ of the different films with the reduced temperature $T-T_{M(e/a)}$. Some evolutions of $L_{(0)}^*$ (N338) and $L_{(1)}^*$ (N283) are also represented. The arrows correspond to $T_C-T_{M(e/a)}$.

Fig. 8: Examples of indention curves P = f(h) for four different temperatures and for the specimen N336. The inset is a zoom of the previous curve over the first 90 nm.

Fig. 9: Young's modulus E versus the Berkovich hardness H_B at ambient temperature for the whole tested films and some values reported in the literature. As deposited and annealed films.

Fig. 10: Hardness at ambient temperature T_a and for the transformation temperature T_M as a function of the $T_a-T_{M(e/a)}$ temperature for all the tested films.

Fig. 11: Planar spacing $d_{(1)}$ and $d_{(2)}$ at room temperature as a function of the hardness H_B for the whole tested films.

Fig. 12: (a) Variations of the Young's modulus versus the T-$T_{M(e/a)}$ reduced temperature for the different tested films. (b) Idem but for the hardness H_B. The arrows correspond to temperature T_C-$T_{M(e/a)}$. Previsions of the model, Eqs.14.

Fig. 13: "Plastic indentation deformation" parameter $H_B/3E$ as a function the T-$T_{M(e/a)}$ reduced temperature for the tested specimens. Existence of a bilinear behavior.

Fig. 14: $H_B/3E$ parameter (idem previous figure) as a function of the planar spacing $d_{(2)}$.

Fig. 15: (a) Examples of magnetization curves $M = f(H_m)$ at different temperatures for the N335 and N336 films. (b) Zoom of the previous figure for the small magnetic fields (N335) and magnetization loops for $-10^3 < H_m < 10^3$ Oe. Prevision of the model, Eq.17.

Fig. 16: Thermo magnetization curves as a function of the reduced temperature, $M = f(T-T_{M(e/a)})$, for the different tested films and for: (a) H_m = 100 Oe, (b) H_m = 1000 Oe. Determination of the Curie temperature T_C.

Fig. 17: (a) Magnetization M of the different films for two temperatures T = -250 and 25 °C and for H_m = 100 and 1000 Oe as a function of temperature parameter T_C-$T_{M(e/a)}$. Existence of a transition at the neighborhood of $T_C = T_{M(e/a)}$. (b) Idem previous figure but versus the planar spacing $d_{(2)}$ and for T = 25 and 45 °C. Existence of a transition at the neighborhood of $T_C=T_{M(e/a)}$.

Fig. 18: (a) Quasi-linear relationship between the magnetization M and the hardness H_B for T = 25 and 45 °C and for H_m = 100 and 1000 Oe. (b) Idem for the $M/H_m^{1/2}$ parameter as a function of the hardness H_B (Eq.18a).

Table I

N	Target Substrate	Composition	e_f (μm)	T_{an} (°C)	t_{an} (h)	Color code
N312	H.P.P., Lesk.0 SiO_2/Si	49.7/26/24.3	~ 3	600	10	purple
N335	Br.M, ILL SiO_2/Si	51.9/26/22.1	~ 2	600	20	green
N330	H.P.P., Lesk.2 SiO_2/Si	53.5/23.5/23	~ 3	600	20	yellow
N333	H.P.P., Lesk.1 SiO_2/Si	53.8/23.3/22.9	~ 3	600	20	pale grey
NE1	H.P.P., Lesk.1 SiO_2/Si	54/22.9/23.1	2.9	600	10	dark maroon
N307	H.P.P., Lesk.0 SiO_2/Si	53.3/24.5/22.2	~ 3	600	20	dark grey
N336	Br.M, ILL SiO_2/Si	54/25/21	1.5	600	20	red
N251	H.P.P., Lesk.0 SiO_2/Si	56.9/21.2/21	1.5	600	20	blue
N283	H.P.P., Lesk.0 Cr/SiO_2/Si	56.5/23.2/20.3	~ 3	600	20	pale green
N338	Br. M., ILL SiO_2/Si	52/26/22	1.5	As deposited	-	dark blue
Bulk	Br. M.	51.2/26.1/22.7	-	As elaborated	-	pale maroon
Other films	Lesk. different targets	different compositions	1.5 to 3	600	10 or 20	black

Table I

The other films (black color) have only been tested at ambient temperature (EDS, XRD and nano-indentation). H.P.P.: Hot Pressed Powder and Br.M.: Bridgman Method.

Table II

N	Composition Ni/Mn/Ga %	e/a	$T_{M(e/a)}$ (°C)	T_C (°C)
N312	49.7/26/24.3	7.519	-58	111
N335	51.9/26/22.1	7.673	50	96
N330	53.5/23.5/23	7.685	59	76
N333	53.8/23.3/22.9	7.698	68	80
NE1	54/22.9/23.1	7.699	69	82
N307	53.3/24.5/22.2	7.711	77	82
N336	54/25/21	7.780	125	82
N251	56.9/21.2/21	7.804	142	80
N283	56.5/23.2/20.3	7.883	198	82
N338	52/26/22	7.680	55	-
Bulk	51.2/26.1/22.7	7.604	19 measured~23	98

Table II

Composition, e/a ratio, martensitic transformation temperature $T_{M(e/a)}$ and Curie temperature Tc

Figure1a,b

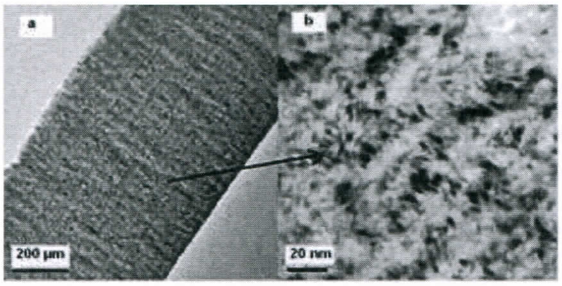

Figure2

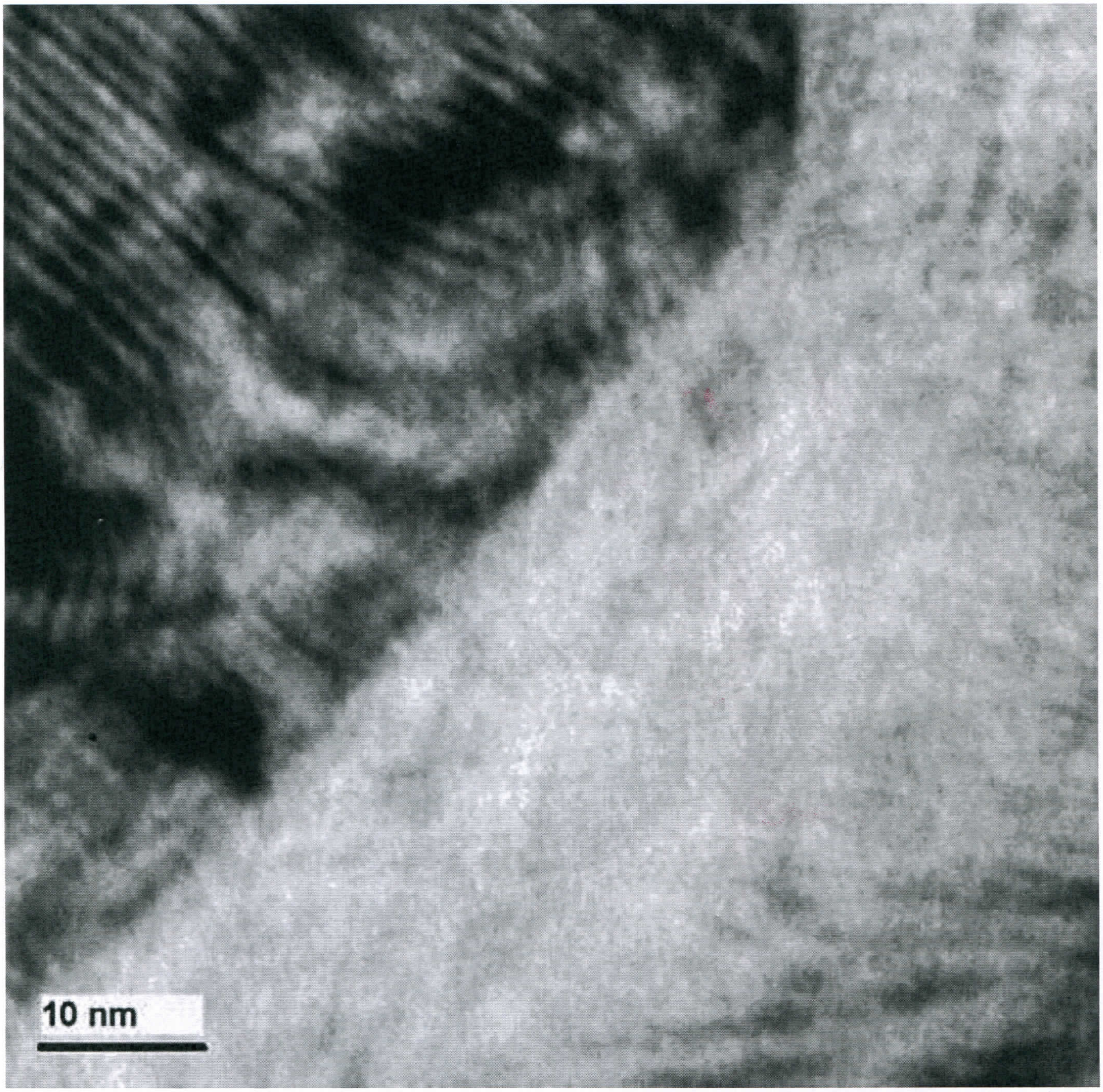

Figure3

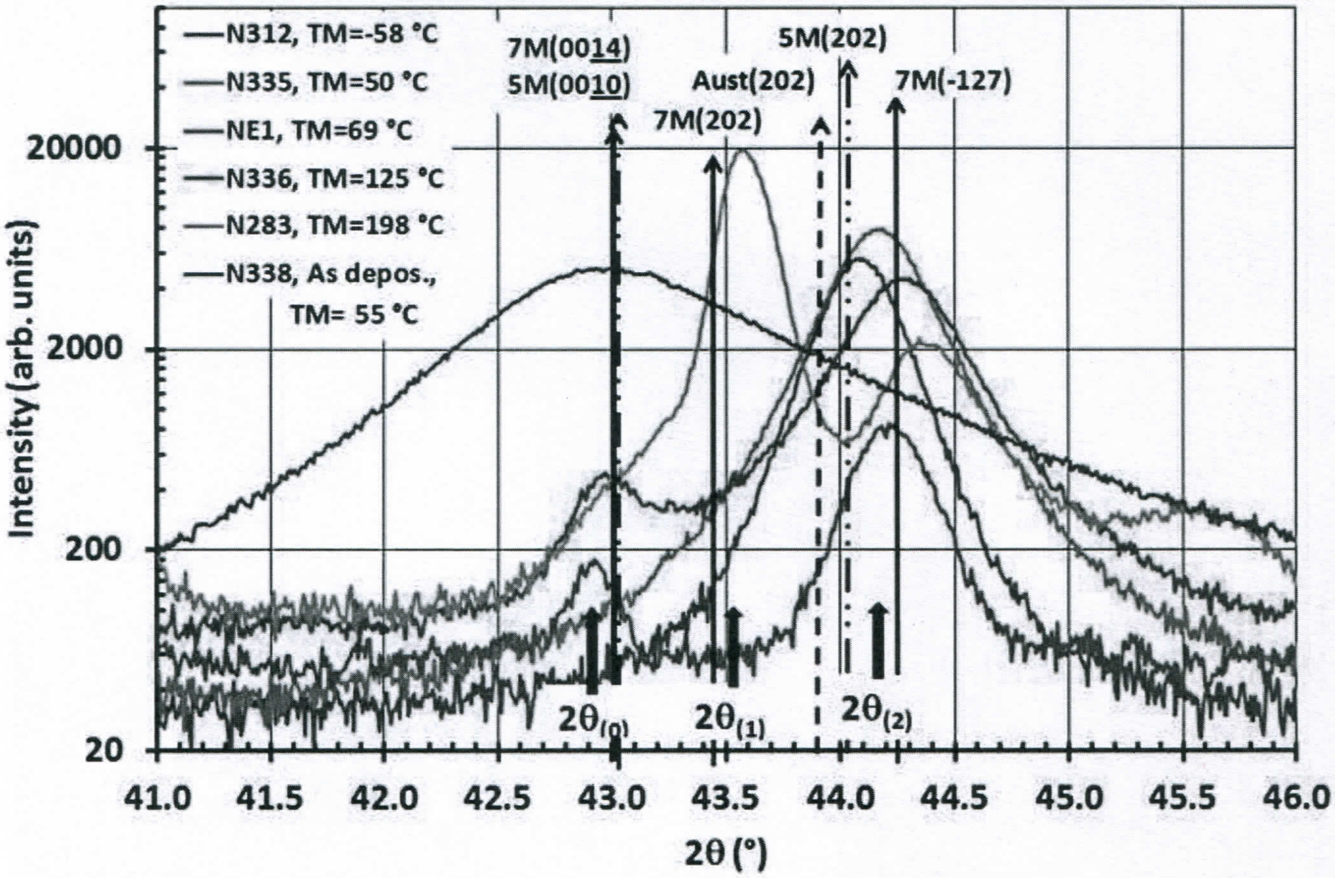
N312, TM=-58 °C
N335, TM=50 °C
NE1, TM=69 °C
N336, TM=125 °C
N283, TM=198 °C
N338, As depos., TM= 55 °C
7M(0014)
5M(0010)
7M(202)
Aust(202)
5M(202)
7M(-127)
$2\theta_{(0)}$
$2\theta_{(1)}$
$2\theta_{(2)}$
Intensity (arb. units)
20
200
2000
20000
41.0
41.5
42.0
42.5
43.0
43.5
44.0
44.5
45.0
45.5
46.0
2θ (°)

Figure4

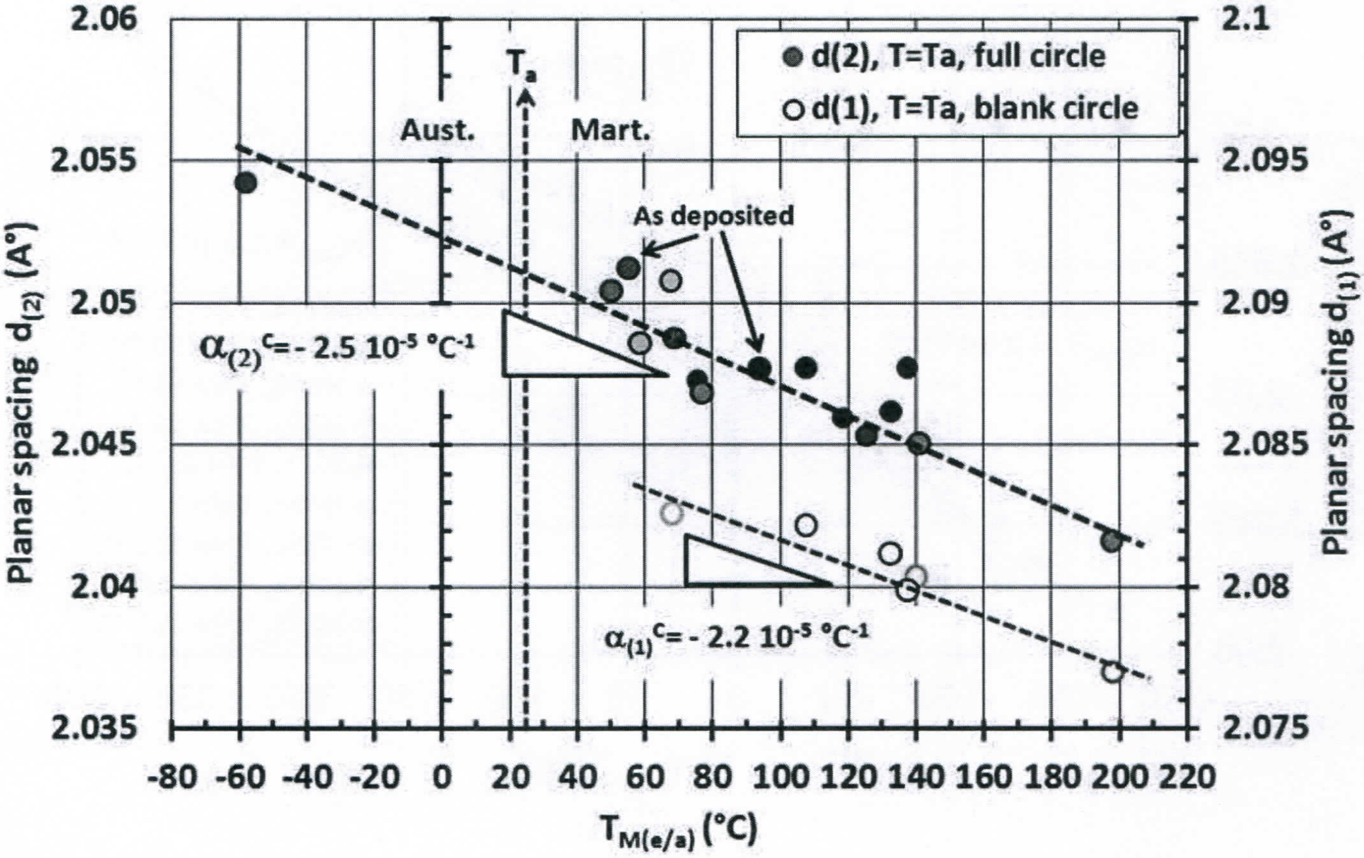

2.06
2.055
2.05
2.045
2.04
2.035
2.1
2.095
2.09
2.085
2.08
2.075
Planar spacing $d_{(2)}$ (A°)
Planar spacing $d_{(1)}$ (A°)
-80 -60 -40 -20 0 20 40 60 80 100 120 140 160 180 200 220
$T_{M(e/a)}$ (°C)
T_a
Aust.
Mart.
As deposited
● d(2), T=Ta, full circle
○ d(1), T=Ta, blank circle
$\alpha_{(2)}^{c}$= - 2.5 10^{-5} °C^{-1}
$\alpha_{(1)}^{c}$= - 2.2 10^{-5} °C^{-1}

Figure5a

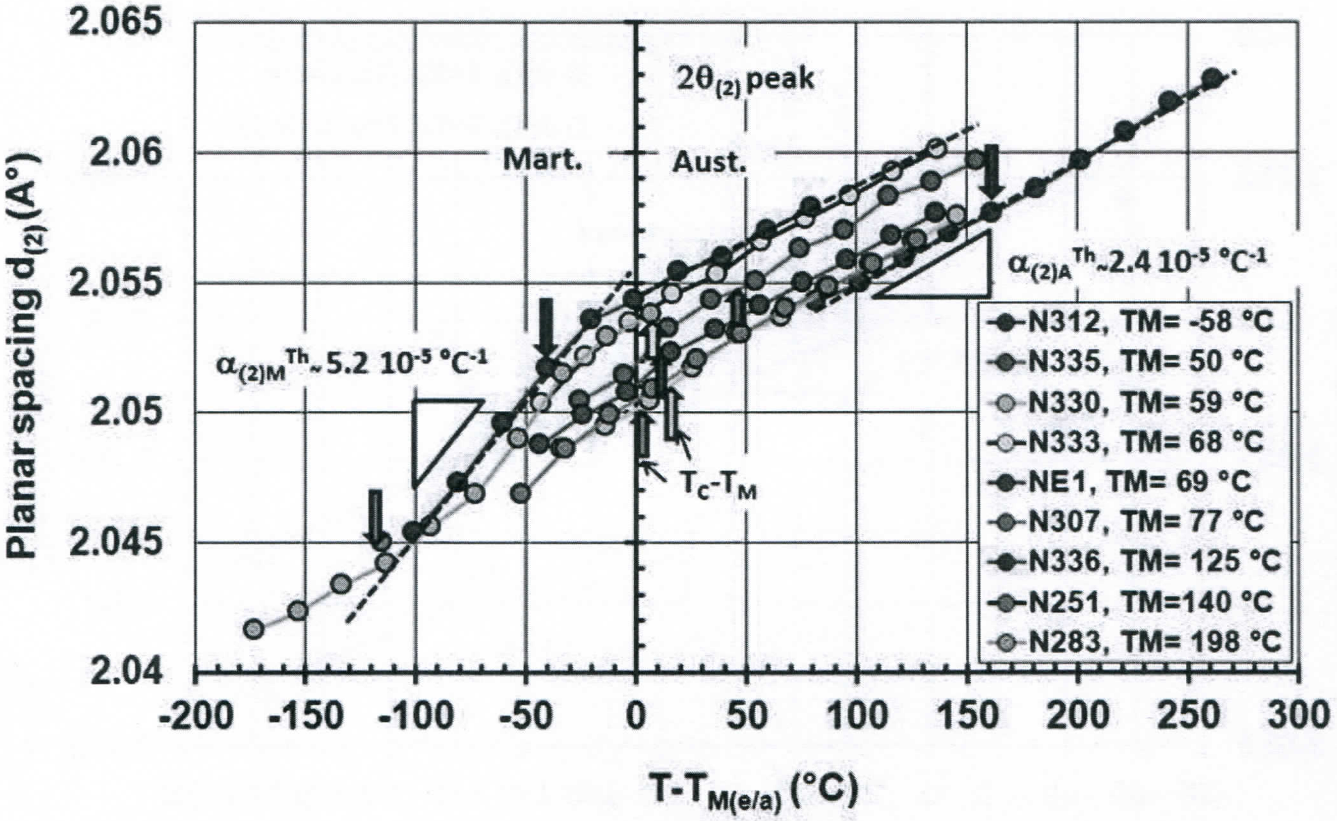
2θ(2) peak
Mart.
Aust.
α(2)M Th ~5.2 10-5 °C-1
α(2)A Th ~2.4 10-5 °C-1
TC-TM
N312, TM= -58 °C
N335, TM= 50 °C
N330, TM= 59 °C
N333, TM= 68 °C
NE1, TM= 69 °C
N307, TM= 77 °C
N336, TM= 125 °C
N251, TM=140 °C
N283, TM= 198 °C
Planar spacing d(2) (A°)
2.065
2.06
2.055
2.05
2.045
2.04
-200
-150
-100
-50
0
50
100
150
200
250
300
T-TM(e/a) (°C)

Figure5b

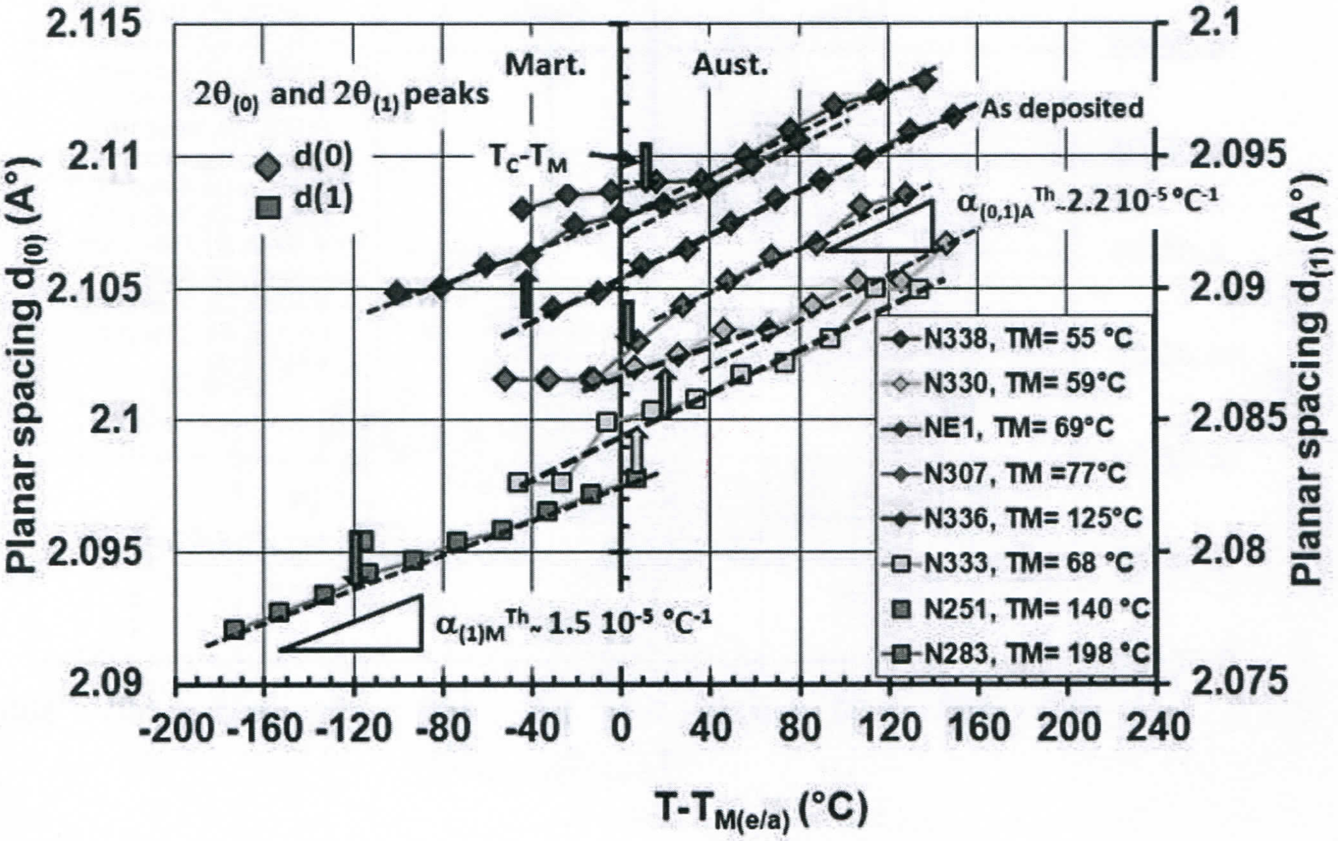

Mart.
Aust.
$2\theta_{(0)}$ and $2\theta_{(1)}$ peaks
d(0)
d(1)
T_C-T_M
As deposited
$\alpha_{(0,1)A}^{Th}$~2.2 10^{-5} °C^{-1}
$\alpha_{(1)M}^{Th}$~ 1.5 10^{-5} °C^{-1}
N338, TM= 55 °C
N330, TM= 59°C
NE1, TM= 69°C
N307, TM =77°C
N336, TM= 125°C
N333, TM= 68 °C
N251, TM= 140 °C
N283, TM= 198 °C
Planar spacing $d_{(0)}$ (A°)
2.115
2.11
2.105
2.1
2.095
2.09
Planar spacing $d_{(1)}$ (A°)
2.1
2.095
2.09
2.085
2.08
2.075
-200
-160
-120
-80
-40
0
40
80
120
160
200
240
T-$T_{M(e/a)}$ (°C)

Figure6

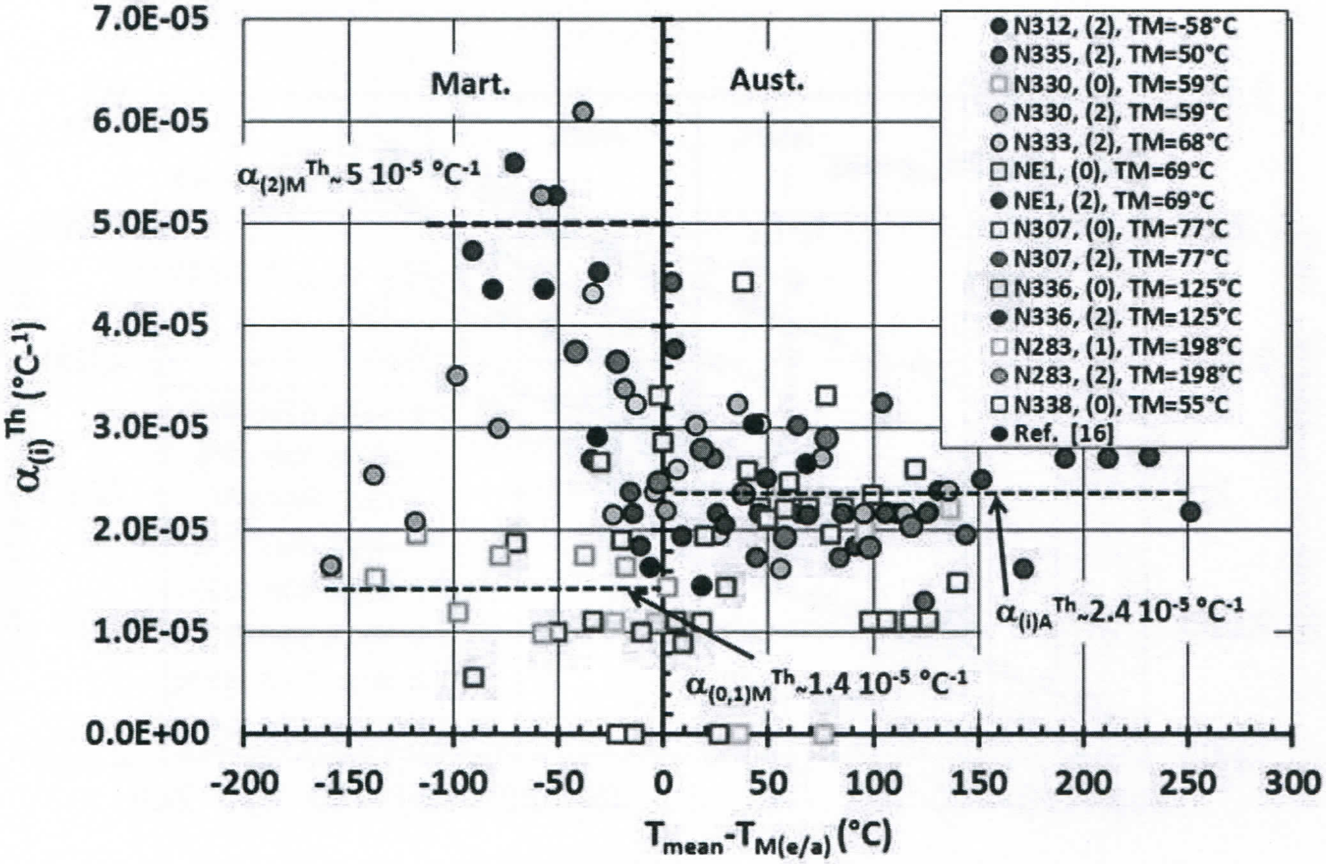
7.0E-05
6.0E-05
5.0E-05
4.0E-05
3.0E-05
2.0E-05
1.0E-05
0.0E+00
$\alpha_{(i)}{}^{Th}$ (°C^{-1})
Mart.
Aust.
$\alpha_{(2)M}{}^{Th}$~5 10^{-5} °C^{-1}
$\alpha_{(0,1)M}{}^{Th}$~1.4 10^{-5} °C^{-1}
$\alpha_{(i)A}{}^{Th}$~2.4 10^{-5} °C^{-1}
● N312, (2), TM=-58°C
● N335, (2), TM=50°C
□ N330, (0), TM=59°C
● N330, (2), TM=59°C
○ N333, (2), TM=68°C
□ NE1, (0), TM=69°C
● NE1, (2), TM=69°C
□ N307, (0), TM=77°C
● N307, (2), TM=77°C
□ N336, (0), TM=125°C
● N336, (2), TM=125°C
□ N283, (1), TM=198°C
● N283, (2), TM=198°C
□ N338, (0), TM=55°C
● Ref. [16]
-200
-150
-100
-50
0
50
100
150
200
250
300
T_{mean}-$T_{M(e/a)}$ (°C)

Figure7

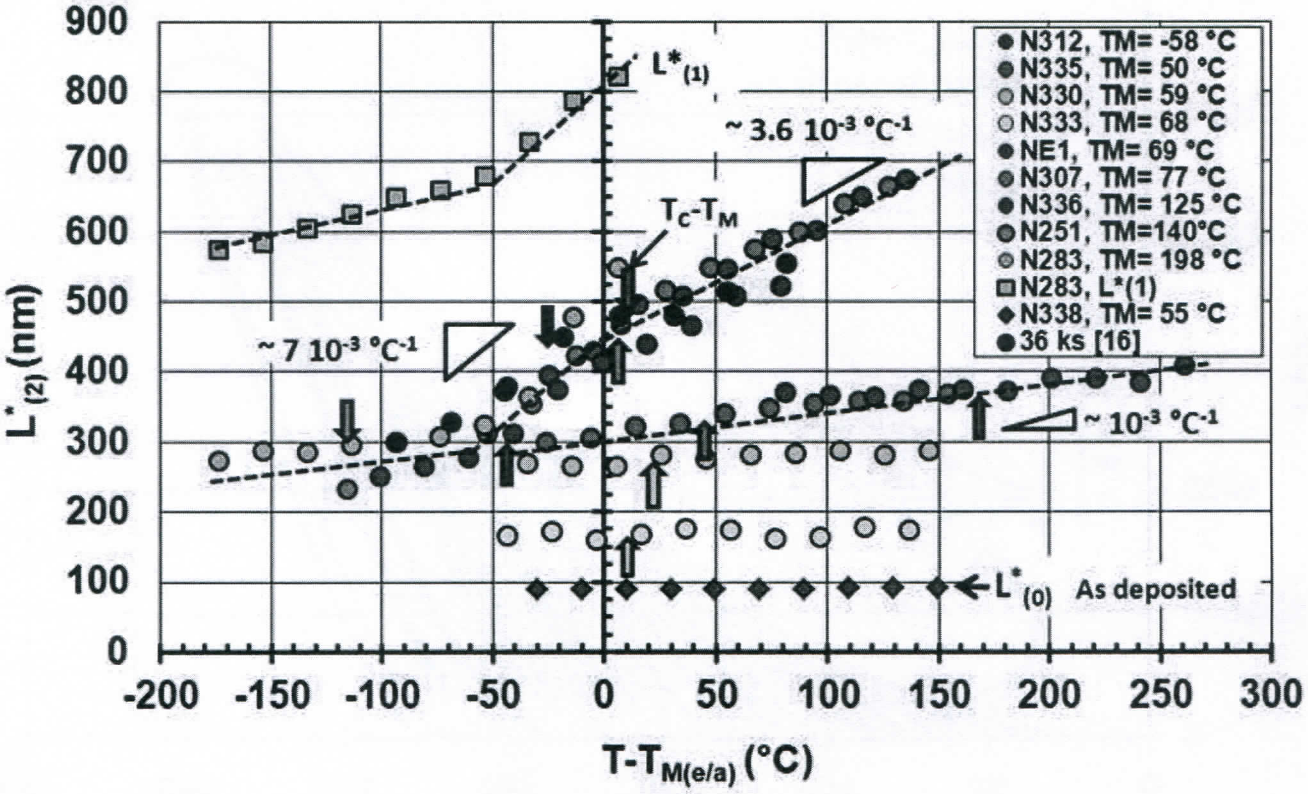

900
800
700
600
500
400
300
200
100
0
$L^*_{(2)}$ (nm)
-200
-150
-100
-50
0
50
100
150
200
250
300
$T-T_{M(e/a)}$ (°C)
$L^*_{(1)}$
~ 3.6 10^{-3} °C^{-1}
T_C-T_M
~ 7 10^{-3} °C^{-1}
~ 10^{-3} °C^{-1}
$L^*_{(0)}$ As deposited
● N312, TM= -58 °C
● N335, TM= 50 °C
● N330, TM= 59 °C
○ N333, TM= 68 °C
● NE1, TM= 69 °C
● N307, TM= 77 °C
● N336, TM= 125 °C
● N251, TM=140°C
● N283, TM= 198 °C
□ N283, L*(1)
◆ N338, TM= 55 °C
● 36 ks [16]

Figure8

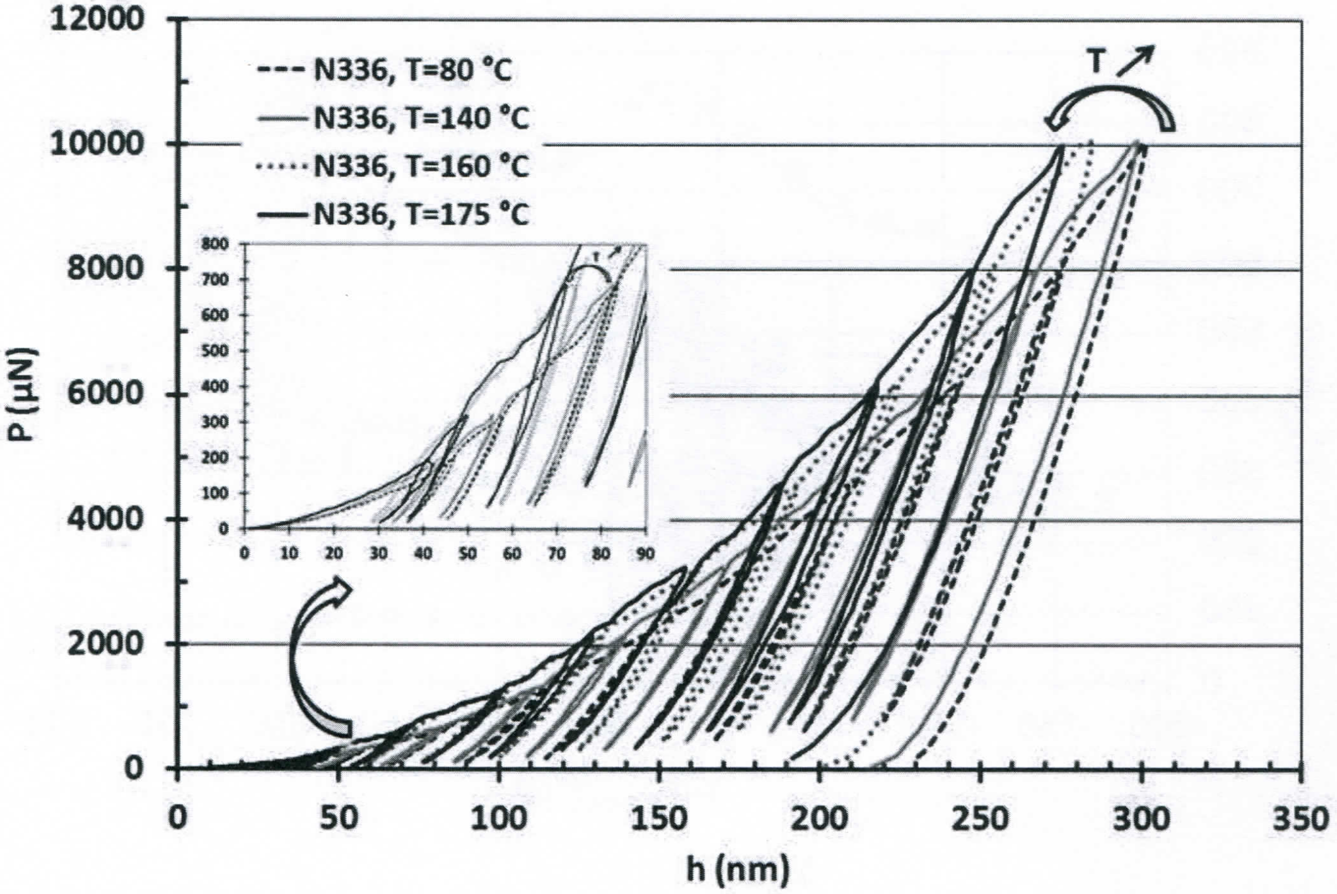
12000
10000
8000
6000
4000
2000
0
P (µN)
0
50
100
150
200
250
300
350
h (nm)
N336, T=80 °C
N336, T=140 °C
N336, T=160 °C
N336, T=175 °C
T ↗
800
700
600
500
400
300
200
100
0
0
10
20
30
40
50
60
70
80
90
T ↗

Figure9

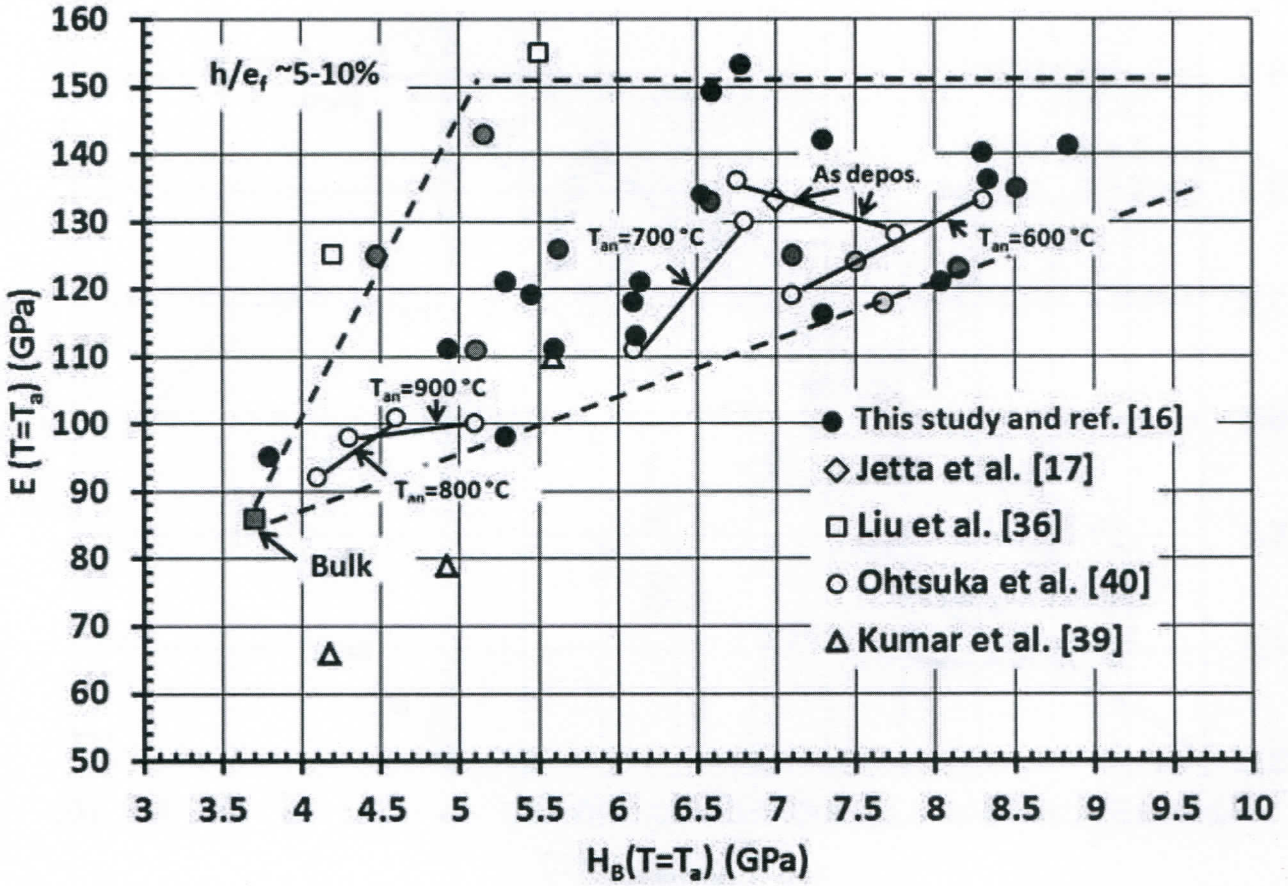
h/e$_f$ ~5-10%
As depos.
T$_{an}$=700 °C
T$_{an}$=600 °C
T$_{an}$=900 °C
T$_{an}$=800 °C
Bulk
● This study and ref. [16]
◇ Jetta et al. [17]
□ Liu et al. [36]
○ Ohtsuka et al. [40]
△ Kumar et al. [39]
E (T=T$_a$) (GPa)
160
150
140
130
120
110
100
90
80
70
60
50
3
3.5
4
4.5
5
5.5
6
6.5
7
7.5
8
8.5
9
9.5
10
H$_B$(T=T$_a$) (GPa)

Figure10

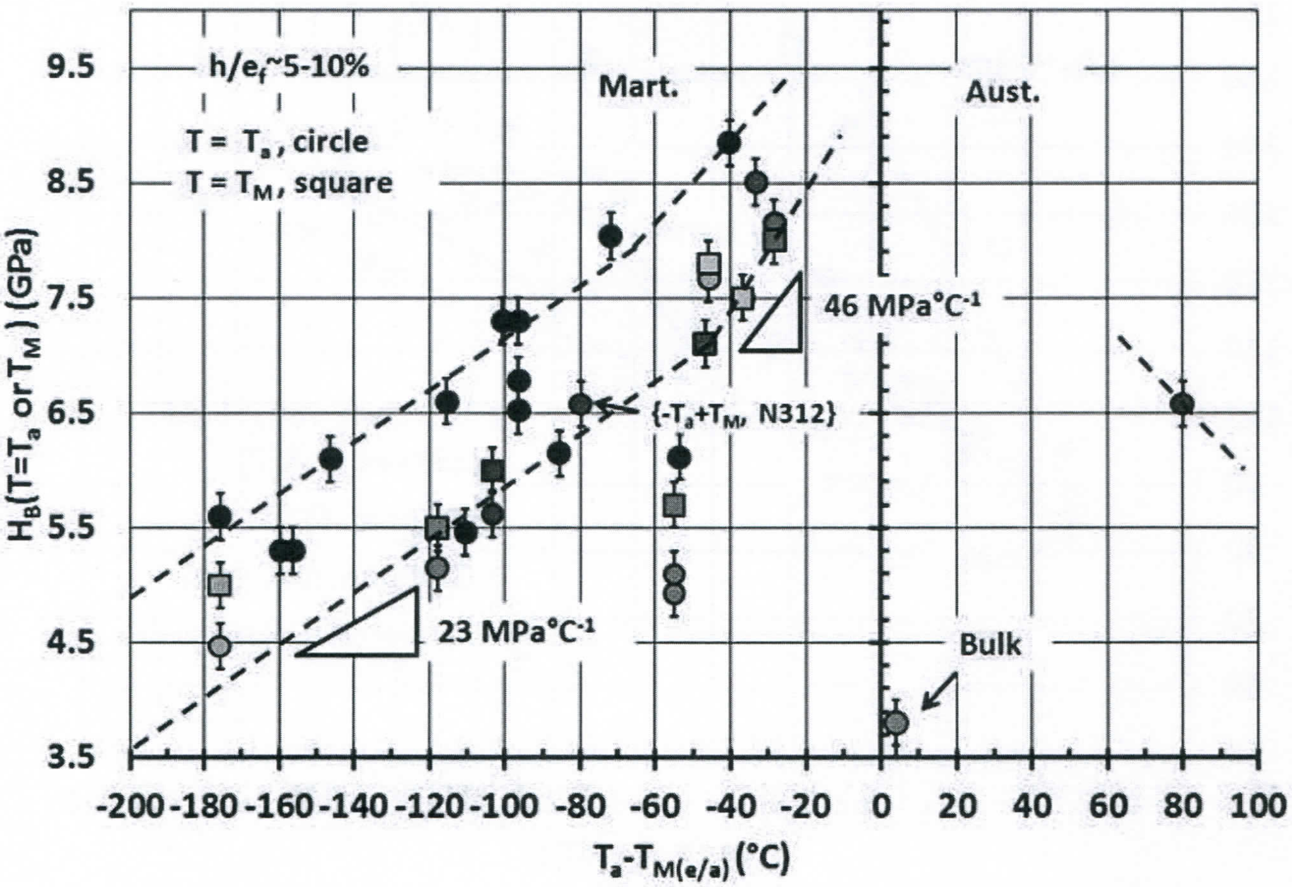
h/e$_f$~5-10%
T = T$_a$, circle
T = T$_M$, square
Mart.
Aust.
46 MPa°C^{-1}
23 MPa°C^{-1}
{-T$_a$+T$_M$, N312}
Bulk
H$_B$(T=T$_a$ or T$_M$) (GPa)
9.5
8.5
7.5
6.5
5.5
4.5
3.5
-200
-180
-160
-140
-120
-100
-80
-60
-40
-20
0
20
40
60
80
100
T$_a$-T$_{M(e/a)}$ (°C)

Figure11

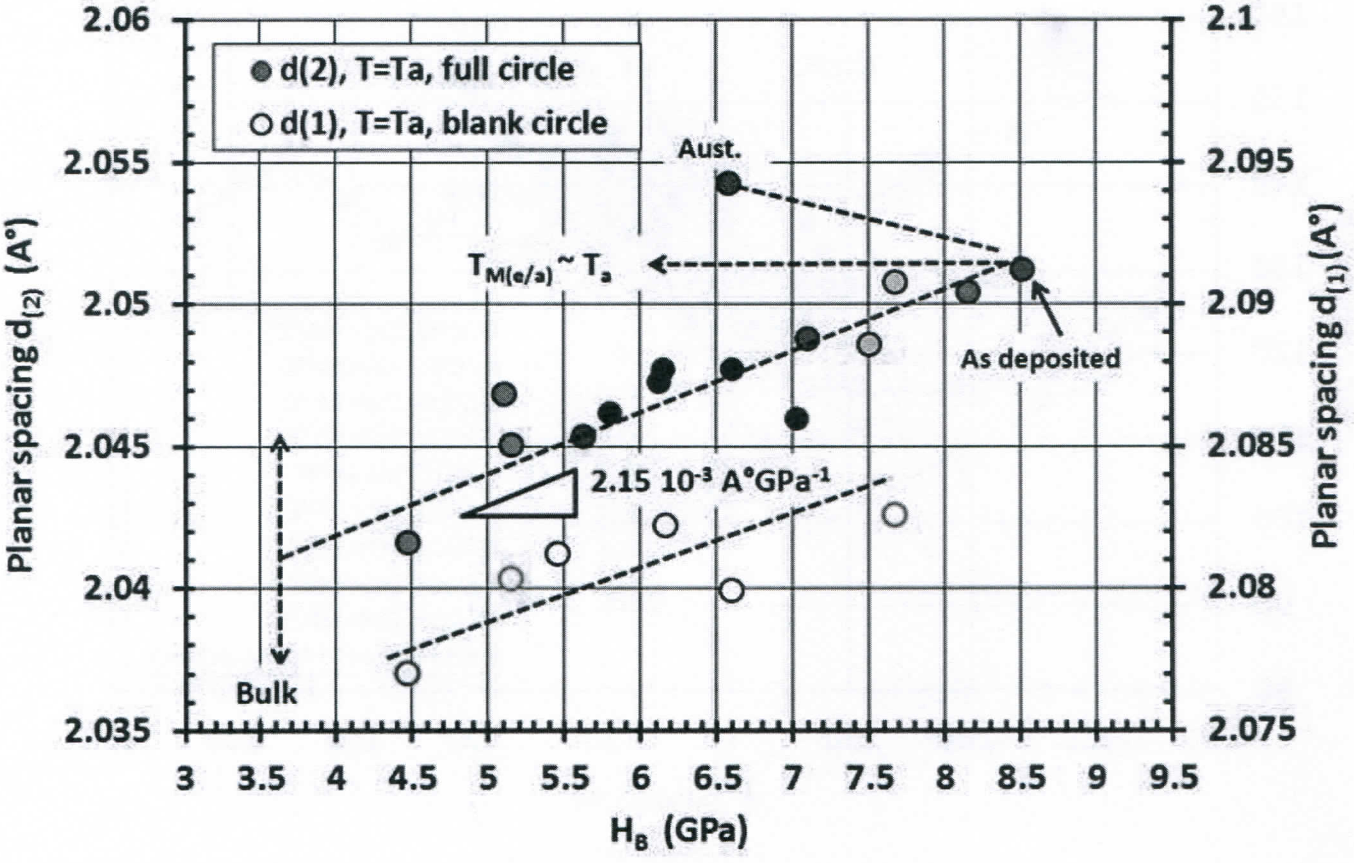
● d(2), T=Ta, full circle
○ d(1), T=Ta, blank circle
Aust.
$T_{M(e/a)}$ ~ T_a
As deposited
2.15 10^{-3} A°GPa^{-1}
Bulk
Planar spacing $d_{(2)}$ (A°)
Planar spacing $d_{(1)}$ (A°)
H_B (GPa)
2.06
2.055
2.05
2.045
2.04
2.035
2.1
2.095
2.09
2.085
2.08
2.075
3
3.5
4
4.5
5
5.5
6
6.5
7
7.5
8
8.5
9
9.5

Figure12a

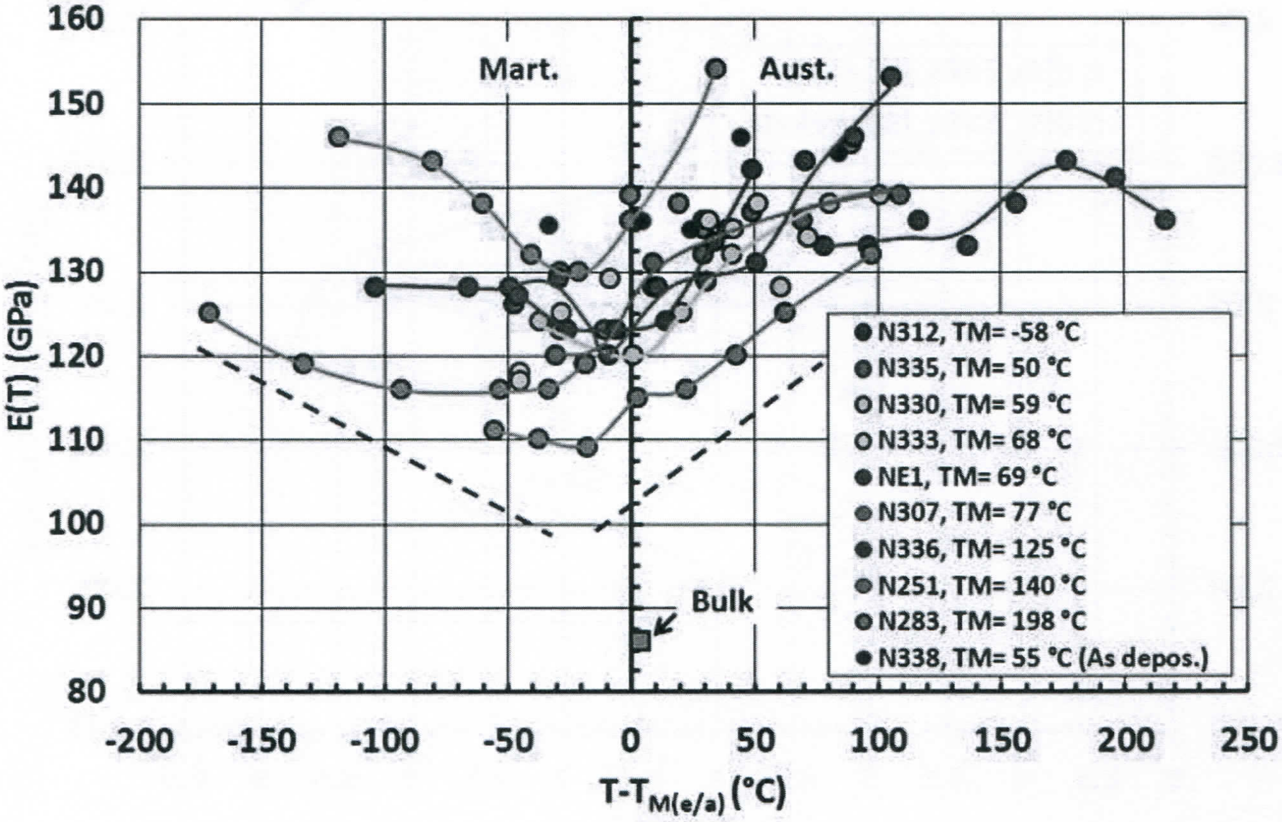
Mart.
Aust.
Bulk
E(T) (GPa)
T-$T_{M(e/a)}$ (°C)
160
150
140
130
120
110
100
90
80
-200
-150
-100
-50
0
50
100
150
200
250
● N312, TM= -58 °C
● N335, TM= 50 °C
○ N330, TM= 59 °C
○ N333, TM= 68 °C
● NE1, TM= 69 °C
● N307, TM= 77 °C
● N336, TM= 125 °C
● N251, TM= 140 °C
● N283, TM= 198 °C
● N338, TM= 55 °C (As depos.)

Figure12b

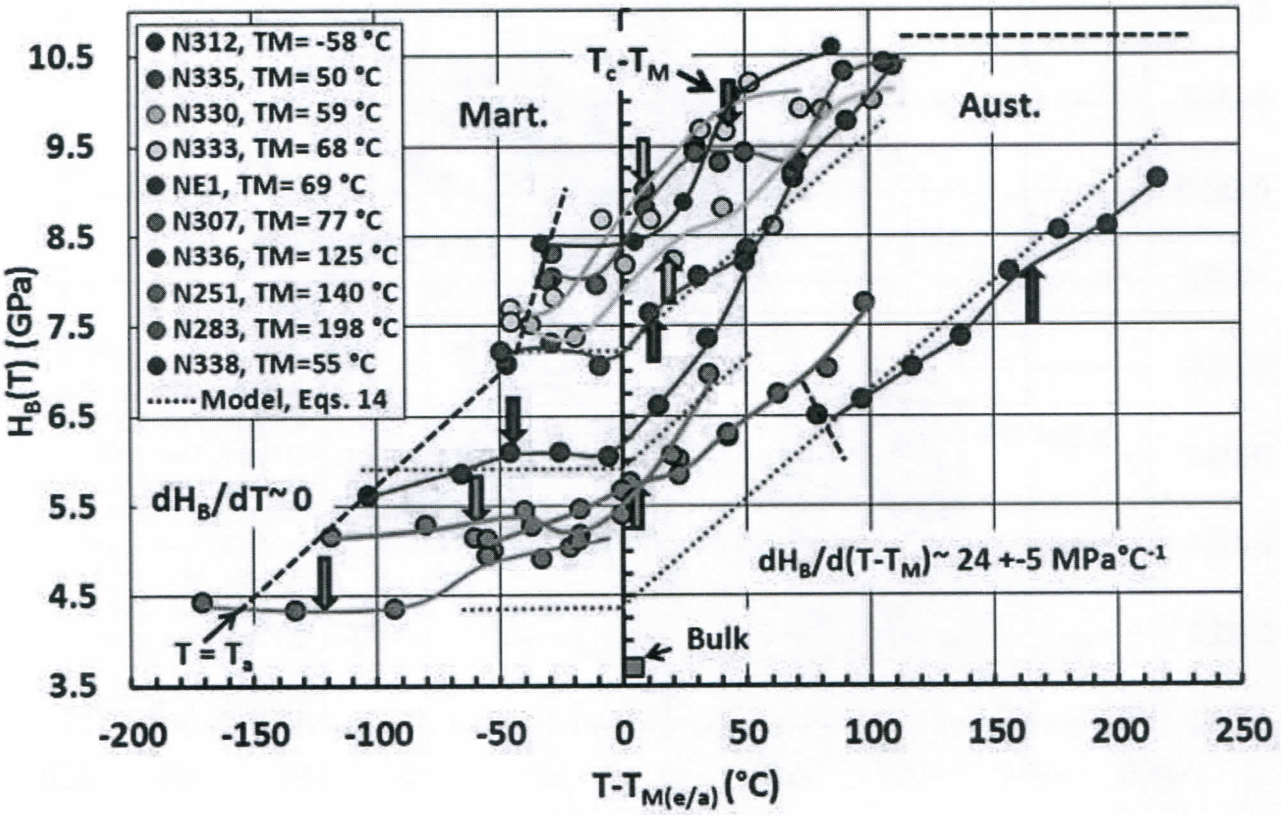
● N312, TM= -58 °C
● N335, TM= 50 °C
● N330, TM= 59 °C
○ N333, TM= 68 °C
● NE1, TM= 69 °C
● N307, TM= 77 °C
● N336, TM= 125 °C
● N251, TM= 140 °C
● N283, TM= 198 °C
● N338, TM=55 °C
······ Model, Eqs. 14
Mart.
Aust.
T_c-T_M
dH_B/dT~ 0
$dH_B/d(T-T_M)$~ 24 +-5 MPa°C^{-1}
$T = T_a$
Bulk
$H_B(T)$ (GPa)
10.5
9.5
8.5
7.5
6.5
5.5
4.5
3.5
-200
-150
-100
-50
0
50
100
150
200
250
T-$T_{M(e/a)}$ (°C)

Figure13

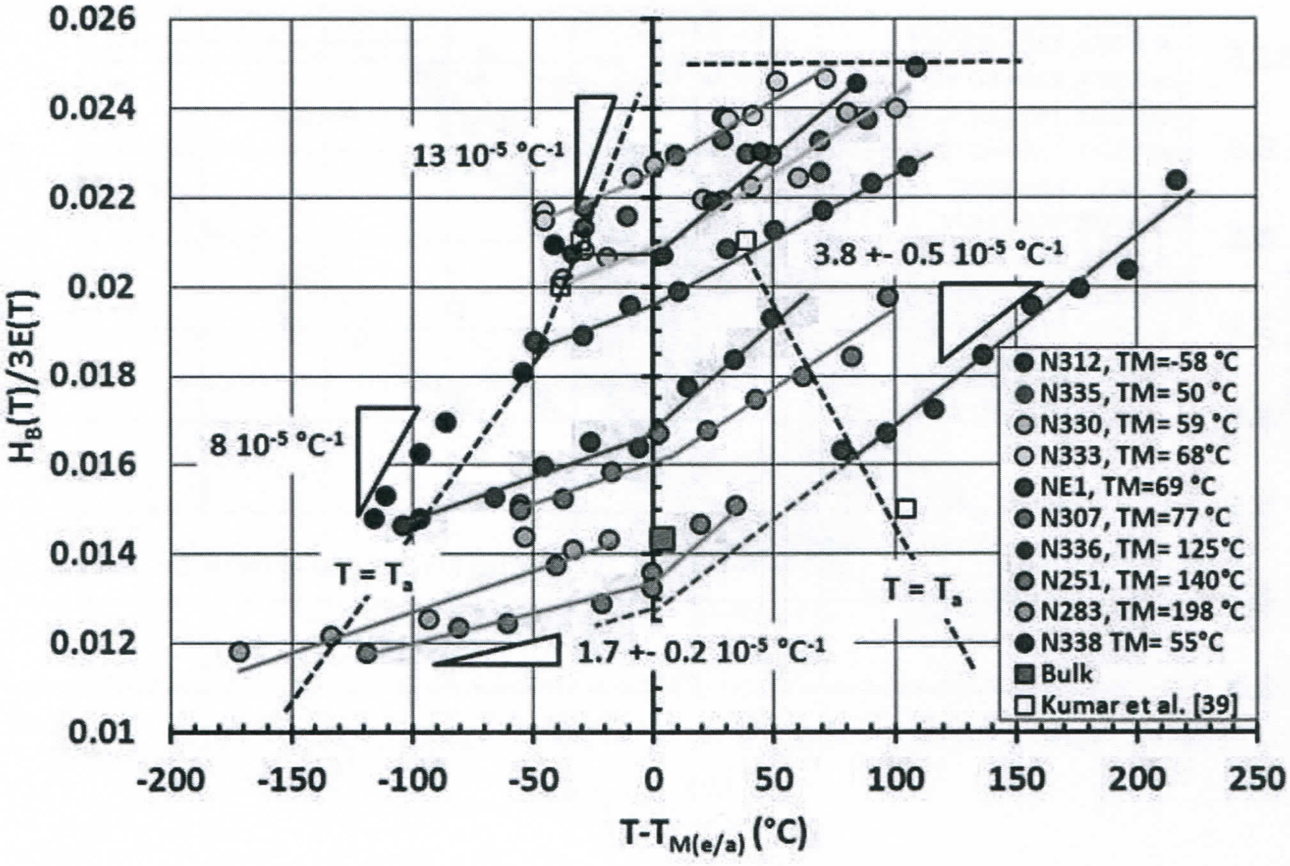
0.026
0.024
0.022
0.02
0.018
0.016
0.014
0.012
0.01
$H_B(T)/3E(T)$
-200
-150
-100
-50
0
50
100
150
200
250
$T-T_{M(e/a)}$ (°C)
13 10^{-5} °C^{-1}
8 10^{-5} °C^{-1}
3.8 +- 0.5 10^{-5} °C^{-1}
1.7 +- 0.2 10^{-5} °C^{-1}
$T = T_a$
$T = T_a$
● N312, TM=-58 °C
● N335, TM= 50 °C
○ N330, TM= 59 °C
○ N333, TM= 68°C
● NE1, TM=69 °C
● N307, TM=77 °C
● N336, TM= 125°C
● N251, TM= 140°C
● N283, TM=198 °C
● N338 TM= 55°C
■ Bulk
☐ Kumar et al. [39]

Figure14

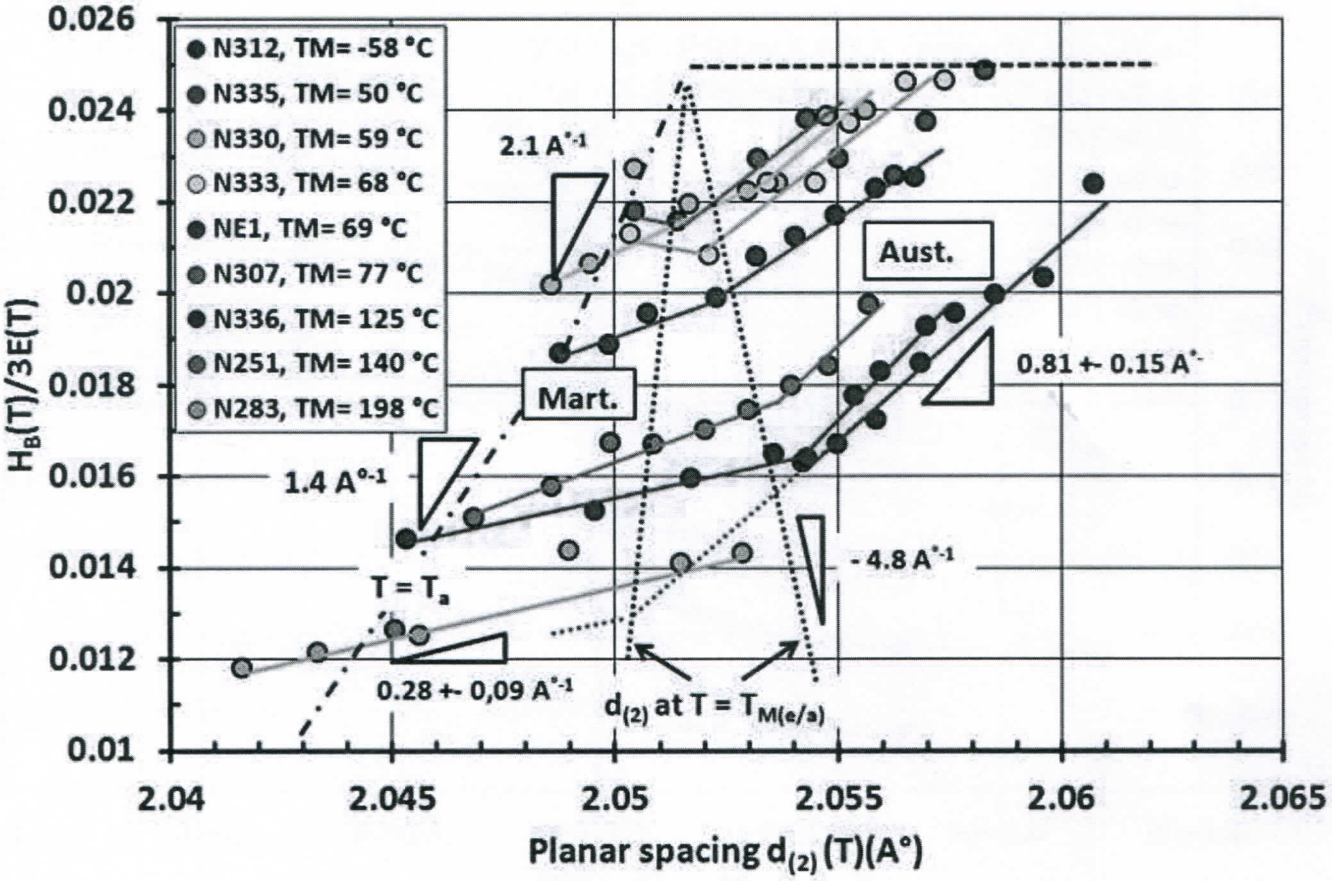

0.026
0.024
0.022
0.02
0.018
0.016
0.014
0.012
0.01
2.04
2.045
2.05
2.055
2.06
2.065
$H_B(T)/3E(T)$
Planar spacing $d_{(2)}(T)$(A°)
● N312, TM= -58 °C
● N335, TM= 50 °C
● N330, TM= 59 °C
○ N333, TM= 68 °C
● NE1, TM= 69 °C
● N307, TM= 77 °C
● N336, TM= 125 °C
● N251, TM= 140 °C
● N283, TM= 198 °C
2.1 A°-1
Aust.
Mart.
0.81 +- 0.15 A°-
1.4 A°-1
T = T_a
- 4.8 A°-1
0.28 +- 0,09 A°-1
$d_{(2)}$ at T = $T_{M(e/a)}$

Figure15a

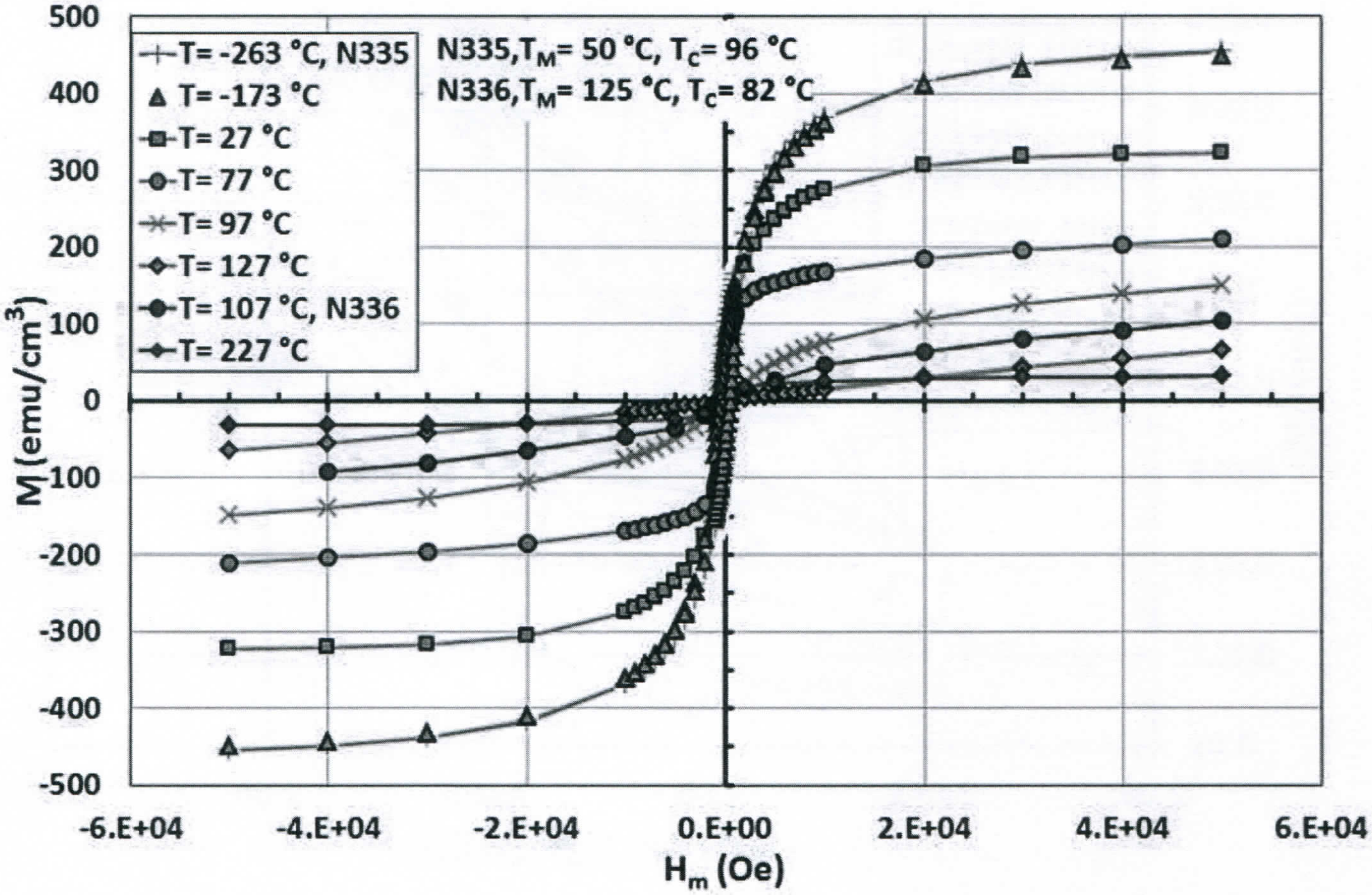

T= -263 °C, N335
T= -173 °C
T= 27 °C
T= 77 °C
T= 97 °C
T= 127 °C
T= 107 °C, N336
T= 227 °C
N335,T_M= 50 °C, T_c= 96 °C
N336,T_M= 125 °C, T_c= 82 °C
500
400
300
200
100
0
-100
-200
-300
-400
-500
M (emu/cm^3)
-6.E+04
-4.E+04
-2.E+04
0.E+00
2.E+04
4.E+04
6.E+04
H_m (Oe)

Figure15b

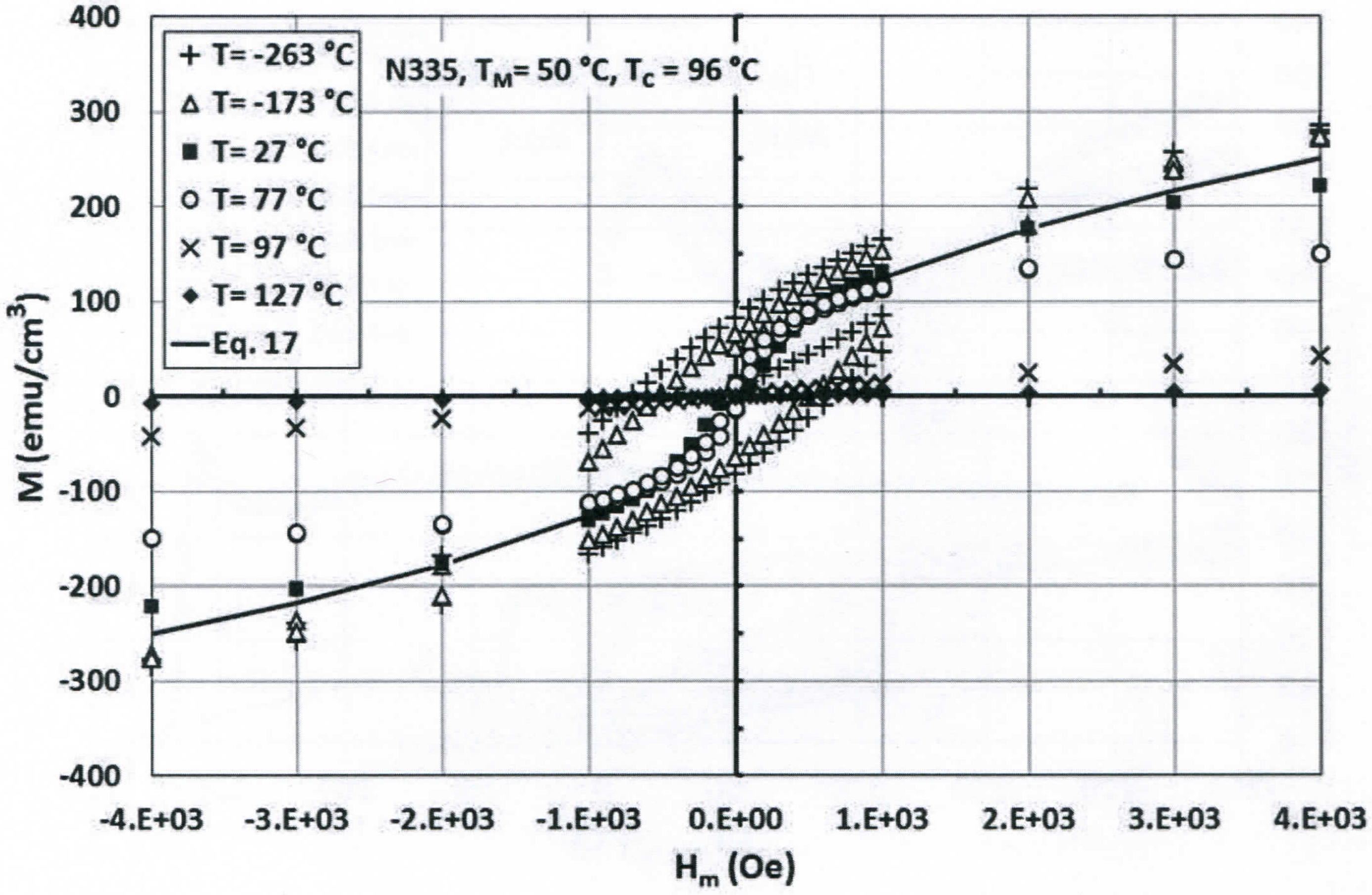
N335, T_M= 50 °C, T_c = 96 °C
+ T= -263 °C
△ T= -173 °C
■ T= 27 °C
○ T= 77 °C
× T= 97 °C
◆ T= 127 °C
—Eq. 17
M (emu/cm^3)
400
300
200
100
0
-100
-200
-300
-400
-4.E+03
-3.E+03
-2.E+03
-1.E+03
0.E+00
1.E+03
2.E+03
3.E+03
4.E+03
H_m (Oe)

Figure 16a

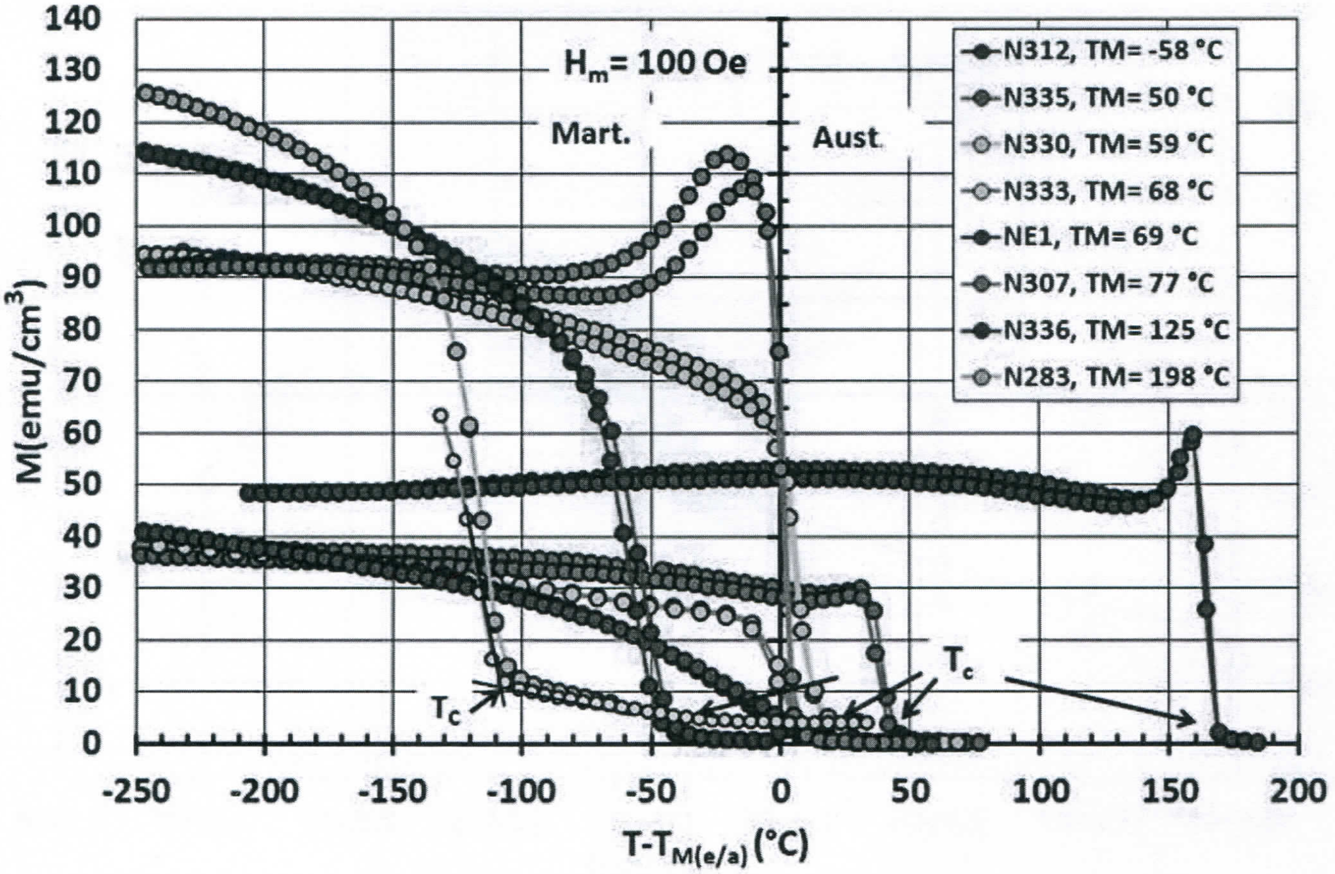
H$_m$= 100 Oe
Mart.
Aust.
N312, TM= -58 °C
N335, TM= 50 °C
N330, TM= 59 °C
N333, TM= 68 °C
NE1, TM= 69 °C
N307, TM= 77 °C
N336, TM= 125 °C
N283, TM= 198 °C
T$_c$
T$_c$
M(emu/cm^3)
140
130
120
110
100
90
80
70
60
50
40
30
20
10
0
-250
-200
-150
-100
-50
0
50
100
150
200
T-T$_{M(e/a)}$ (°C)

Figure 16b

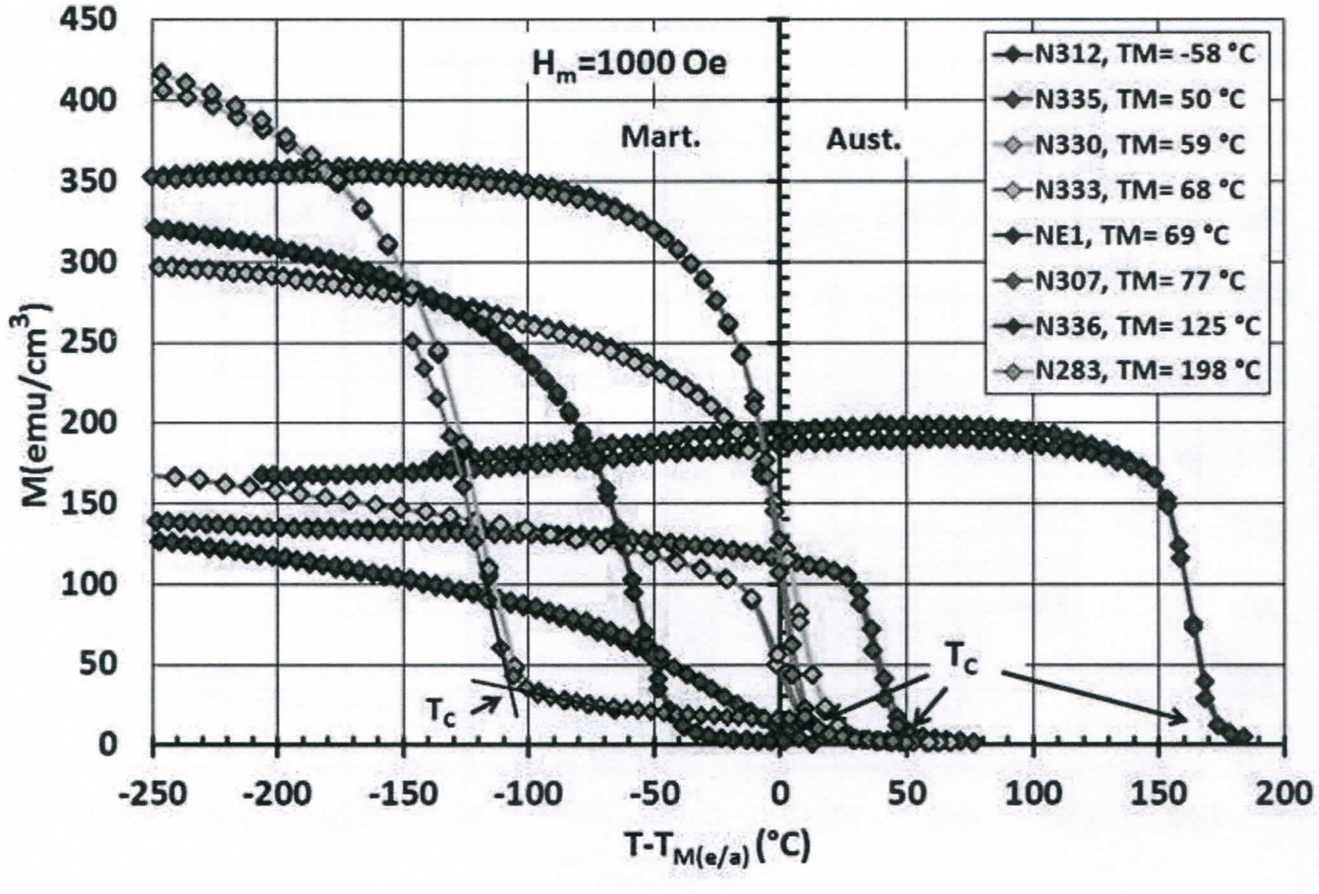
H_m=1000 Oe
Mart.
Aust.
N312, TM= -58 °C
N335, TM= 50 °C
N330, TM= 59 °C
N333, TM= 68 °C
NE1, TM= 69 °C
N307, TM= 77 °C
N336, TM= 125 °C
N283, TM= 198 °C
T_C
T_C
M(emu/cm³)
450
400
350
300
250
200
150
100
50
0
-250
-200
-150
-100
-50
0
50
100
150
200
T-T_M(e/a) (°C)

Figure17a

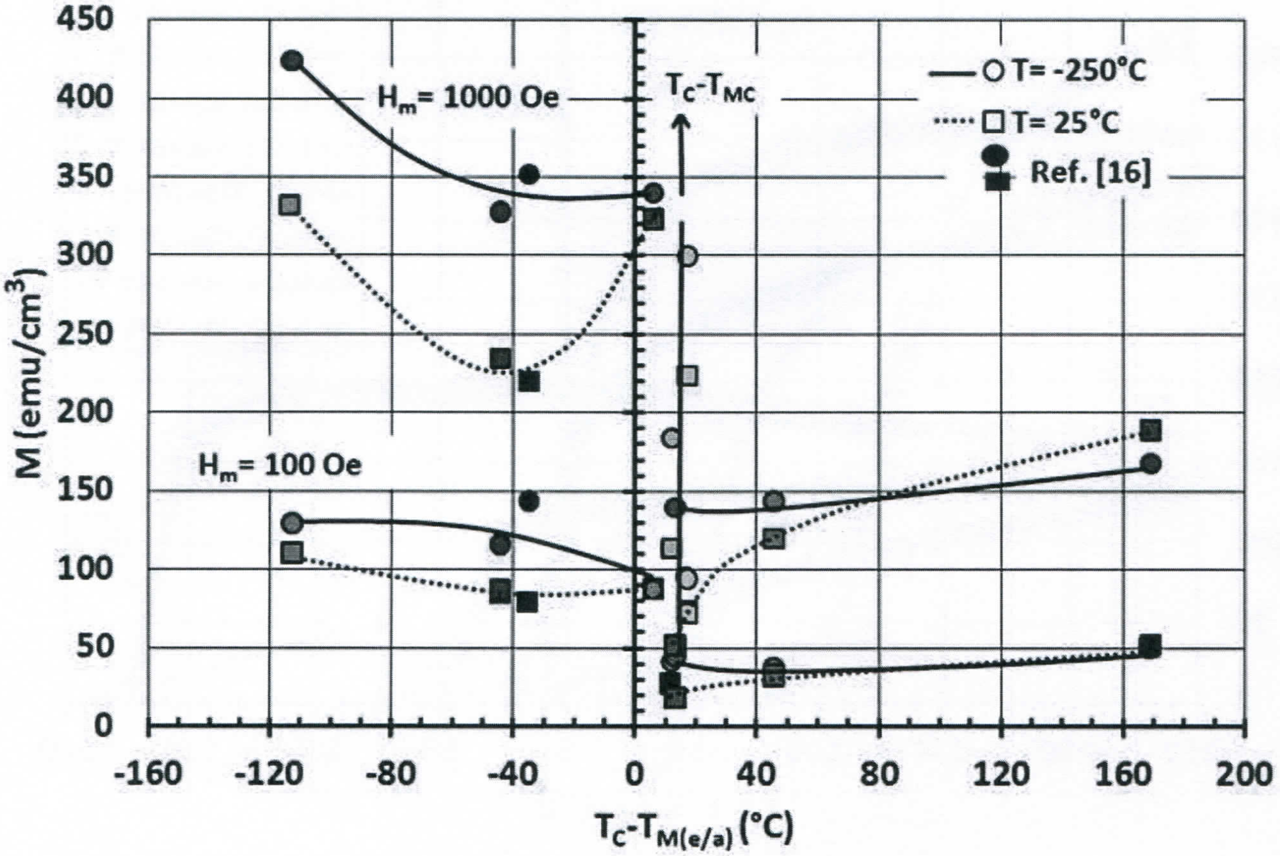
H$_m$= 1000 Oe
H$_m$= 100 Oe
T$_C$-T$_{MC}$
T= -250°C
T= 25°C
Ref. [16]
M (emu/cm^3)
450
400
350
300
250
200
150
100
50
0
-160
-120
-80
-40
0
40
80
120
160
200
T$_C$-T$_{M(e/a)}$ (°C)

Figure17b

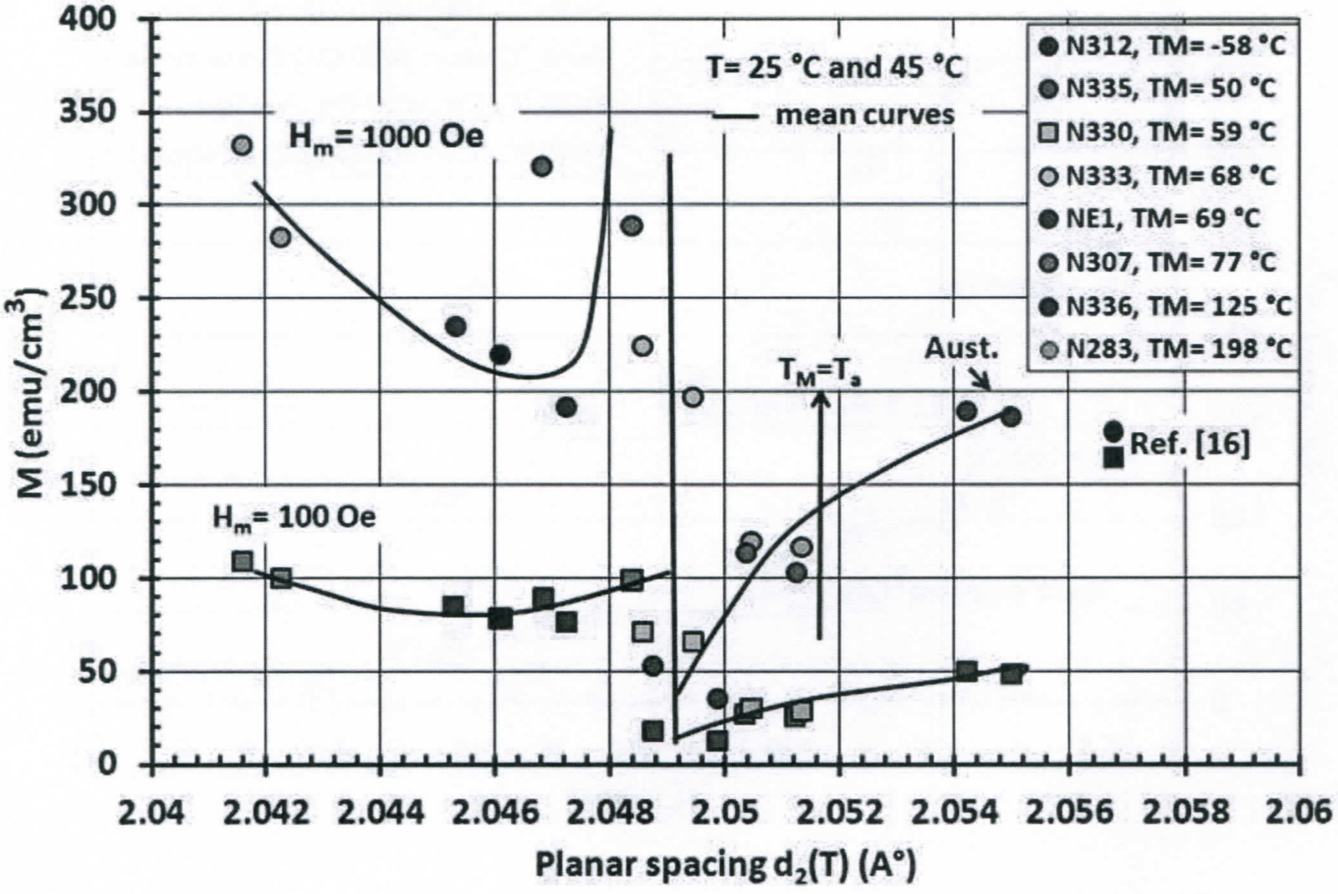

400
350
300
250
200
150
100
50
0
M (emu/cm^3)
2.04
2.042
2.044
2.046
2.048
2.05
2.052
2.054
2.056
2.058
2.06
Planar spacing d_2(T) (A°)
H_m= 1000 Oe
H_m= 100 Oe
T= 25 °C and 45 °C
— mean curves
T_M=T_a
Aust.
Ref. [16]
● N312, TM= -58 °C
● N335, TM= 50 °C
□ N330, TM= 59 °C
○ N333, TM= 68 °C
● NE1, TM= 69 °C
● N307, TM= 77 °C
● N336, TM= 125 °C
○ N283, TM= 198 °C

Figure18a

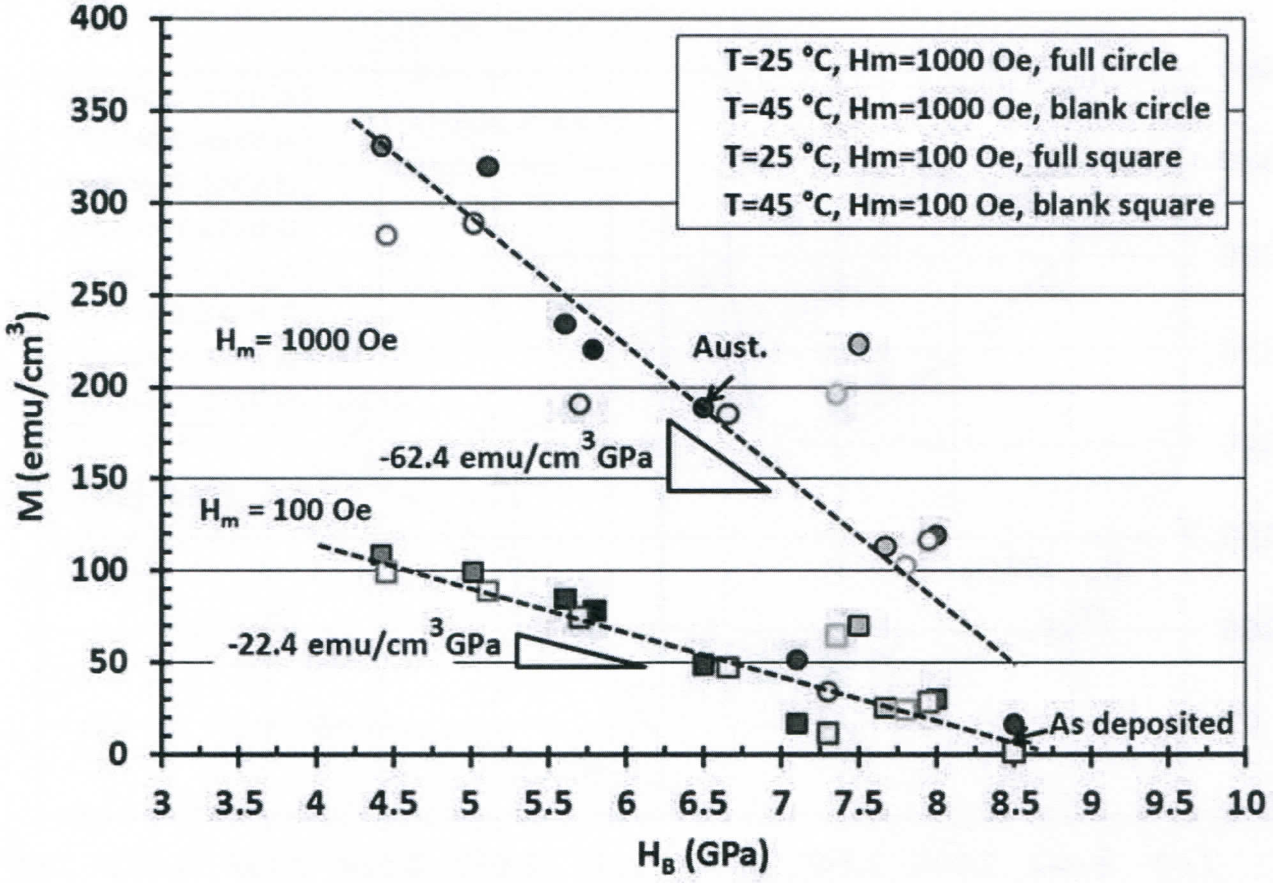
T=25 °C, Hm=1000 Oe, full circle
T=45 °C, Hm=1000 Oe, blank circle
T=25 °C, Hm=100 Oe, full square
T=45 °C, Hm=100 Oe, blank square
H_m= 1000 Oe
Aust.
-62.4 emu/cm^{3}GPa
H_m = 100 Oe
-22.4 emu/cm^{3}GPa
As deposited
M (emu/cm^3)
H_B (GPa)
400
350
300
250
200
150
100
50
0
3
3.5
4
4.5
5
5.5
6
6.5
7
7.5
8
8.5
9
9.5
10

Figure18b

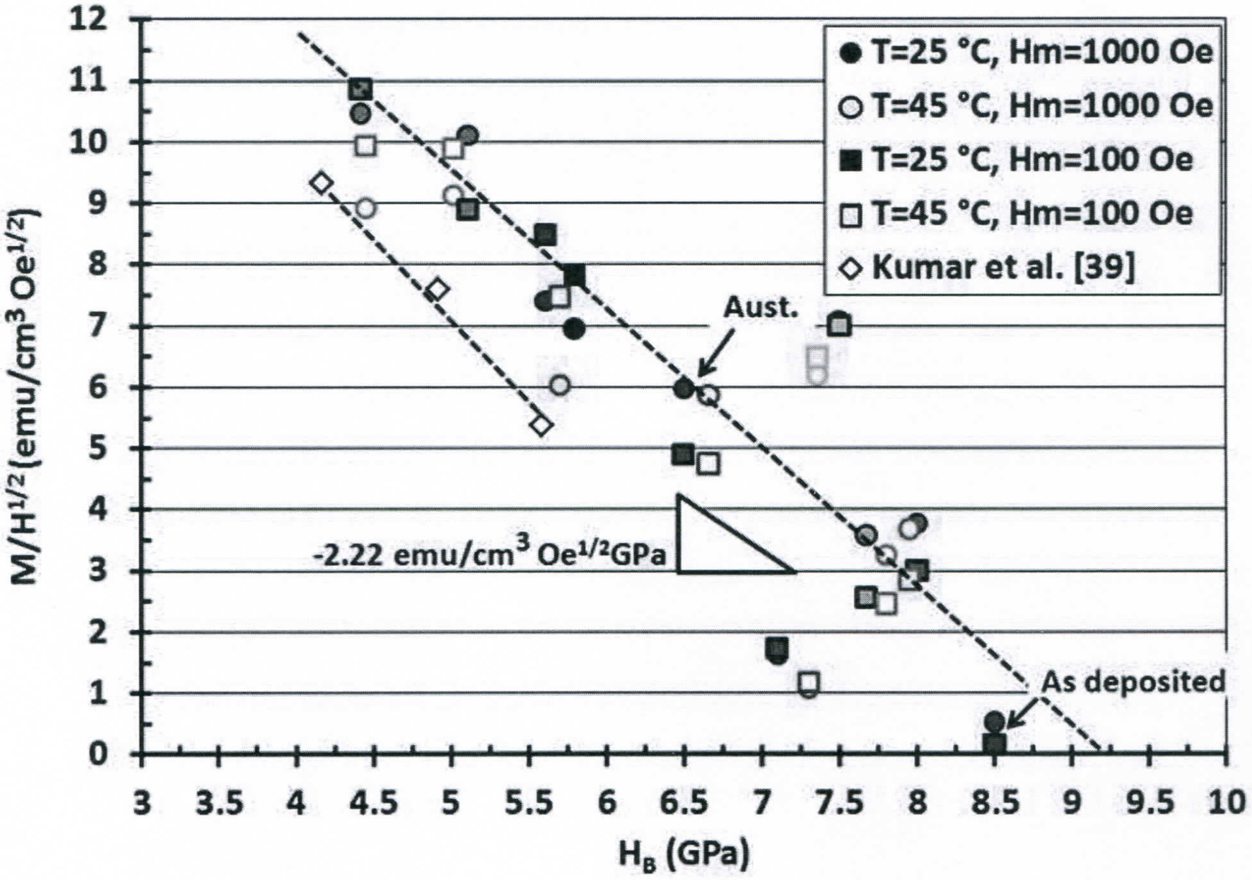

● T=25 °C, Hm=1000 Oe
○ T=45 °C, Hm=1000 Oe
■ T=25 °C, Hm=100 Oe
□ T=45 °C, Hm=100 Oe
◇ Kumar et al. [39]
Aust.
As deposited
-2.22 emu/cm^3 Oe$^{1/2}$GPa
M/H$^{1/2}$ (emu/cm^3 Oe$^{1/2}$)
H$_B$ (GPa)
0
1
2
3
4
5
6
7
8
9
10
11
12
3
3.5
4
4.5
5
5.5
6
6.5
7
7.5
8
8.5
9
9.5
10